JCB Journal of Cell Biology

ARTICLE

Polyploidy reprograms epithelial cells for motility and phagocytosis via stress signaling

Youfang Zhou[1*], Xianfeng Wang[1*], Xiaochao Tan[2], Shingo Nara[3], Yi-Chun Huang[1], Yoichiro Tamori[3,4], and Wu-Min Deng[1]

Polyploidy, an increase in cellular genome content, is a conserved developmental program and a hallmark of malignant cancer, yet its impact on cell behavior remains poorly understood. Here, we show that induction of polyploidy in otherwise diploid cells causes intrinsic stress that reprograms cellular physiology to promote motility-like and phagocytic behaviors. Using the *Drosophila* wing imaginal disc, we find that induced polyploidy enhances membrane dynamics and triggers dynamic cell behavior through a ROS–JNK stress axis activated by ER stress. These cells also acquire phagocytic activity, engulfing both dead and live neighboring cells in developmental and tumor contexts. This stress-induced reprogramming is conserved in induced poly-aneuploid mammalian cancer cells, linking increased genomic content to metastatic traits. Our findings uncover a conserved role for induced polyploidy in driving stress-responsive and immune cell–like behaviors, revealing how elevated ploidy can reshape epithelial function during development and disease.

Introduction

Polyploidy is widely observed in plants and animals and plays an essential role in normal development, injury response, and tumor progression in metazoans (Anatskaya and Vinogradov, 2022; Gjelsvik et al., 2019; Peterson and Fox, 2021). In normal development, cells become polyploid to increase organ and tissue size, as seen in hepatocytes and cardiomyocytes in the mammalian liver and heart (Donne et al., 2020; Elia et al., 2023). After injury, polyploid cells frequently emerge and help facilitate wound repair by enhancing tissue regeneration (Losick et al., 2013). Polyploidy is also a hallmark of cancer, found in various tumor types where it contributes to increased tumor heterogeneity and therapeutic resistance (Duncan et al., 2010; Herriage et al., 2024; Moein et al., 2020; Pienta et al., 2022; Wang et al., 2021). By enhancing cellular plasticity, polyploid cells may serve as a reservoir of cancer stem cells, driving tumor evolution and the persistence of aggressive cell populations (Liu et al., 2024; Moein et al., 2020). Additionally, polyploid cells exhibit enhanced resistance to environmental stress, contributing to their survival under adverse conditions, including radiation and hypoxia (Anatskaya and Vinogradov, 2022; Moein et al., 2020; Wang and Tamori, 2024).

Polyploidy occurs throughout all developmental stages in *Drosophila*. For example, larval salivary gland cells undergo endoreplication, producing polytene chromosomes that have been used to analyze chromatin structure and visualize genome-wide, site-specific chromatin protein binding (Johansen et al., 2009; Paro, 2008). In the transition zone of the salivary gland imaginal ring, polyploid cells can drive tumor growth and genomic instability (Wang et al., 2021). Additionally, polyploid fat body cells in larvae secrete Dilp6, an insulin-like peptide that promotes whole-body growth during the late stages of larval development (Okamoto et al., 2009; Slaidina et al., 2009). In the adult fly brain, several types of neurons and glial cells become polyploid, which helps protect against DNA damage-induced cell death (Nandakumar et al., 2020). In the ovary, both nurse cells and follicle cells become polyploid and play important roles in germline development (Buszczak and Cooley, 2000). Recently, we showed that polyploidy in follicle cells is required for their efficient transformation into nonprofessional phagocytes (NPPs) under stress conditions (Huang et al., 2025). Moreover, wound-induced polyploidy and endoreplication-mediated compensatory cellular hypertrophy are critical for wound healing and tissue homeostasis in postmitotic adult tissues (Losick, 2016; Tamori and Deng, 2013; Tamori and Deng, 2014).

One of the most common mechanisms for generating polyploidy is the endocycle, in which cells skip the mitotic phase of the cell cycle and instead undergo endoreplication (Wang and Tamori, 2024). Fizzy-related (*fzr*), the *Drosophila* homolog to mammalian Cdh1, plays a central role in this process. Fzr associates with the anaphase-promoting complex/cyclosome to promote the ubiquitin-mediated degradation of cyclin B1, thereby preventing entry into mitosis and enabling polyploid

[1]Department of Biochemistry and Molecular Biology, Tulane Cancer Center, Tulane University School of Medicine, New Orleans, LA, USA; [2]Department of Medicine, Louisiana Cancer Research Center, Tulane University School of Medicine, New Orleans, LA, USA; [3]Department of Molecular Oncology, Kyoto University Graduate School of Medicine, Kyoto, Japan; [4]Department of Biology, University of Louisiana at Lafayette, Lafayette, LA, USA.

*Y. Zhou and X. Wang contributed equally to this paper. Correspondence to Wu-Min Deng: wdeng7@tulane.edu.

https://doi.org/10.1083/jcb.202507096

cell formation (Schaeffer et al., 2004; Shcherbata et al., 2004). Interestingly, imaginal wing disc cells overexpressing *fzr* exhibit strong resistance to radiation; although they initially undergo apoptosis following irradiation, they survive and recover within 24 h (Wang and Tamori, 2024). Another regulator, roughex (*rux*), a cyclin A inhibitor, also induces polyploidy when overexpressed. However, *rux*-induced polyploid cells undergo a reversible senescence and heterogeneous cell cycle arrest, leading to severe tissue undergrowth after an initial increase in size (Huang et al., 2024).

Using the *Drosophila* wing imaginal disc, a well-established model for studying organ growth and size control (Alexandre et al., 2014; Tripathi et al., 2022), which typically expands through increased cell number while remaining diploid, we examined how polyploidy promotes dynamic cellular behaviors. We found that inducing polyploidy in wing disc cells activates JNK signaling through elevated levels of reactive oxygen species (ROS), leading to motility-associated cellular behaviors. These induced polyploid cells also acquire phagocytic capability, enabling them to engulf neighboring cells. Together, these findings suggest that induced polyploidy induces a stress-like state that drives immune cell–like behaviors in both developmental contexts and the tumor microenvironment.

Results

Induced polyploidy enhances cell dynamics in the wing imaginal disc and border cells

To determine how increased ploidy alters cellular behavior, we overexpressed *fzr* (*fzr-OE*) or *rux* (*rux-OE*) (Huang et al., 2024; Schaeffer et al., 2004) (Fig. S1 A) to induce polyploidy in the posterior compartment of the wing imaginal disc using hedgehog *(hh)-Gal4* (Tripathi et al., 2022) with a *tub-Gal80^{ts}* to provide the temporally control of gene expression (*hh^{ts}>Gal4*). Consistent with previous reports that unscheduled polyploidy causes tissue undergrowth (Huang et al., 2024), we observed a reduction in the size of the posterior compartment. Notably, GFP-marked polyploid cells were detected in the anterior compartment (Fig. 1, A and B), suggesting that induced polyploid cells can cross the anterior-posterior (AP) boundary. In contrast, diploid cells expressing only *hh>GFP* remained confined to the posterior compartment and never crossed the boundary. Furthermore, knockdown of *fzr* or *rux* using *fzr RNAi* or *rux RNAi* in the posterior compartment, although it also led to a reduction in tissue size, the cells remained restricted to their original location (Fig. S1 B). These results suggest that induced polyploidy promotes dynamic behavior that enables cells to across the compartment boundaries.

To confirm the motility-like, dynamic behavior of polyploid cells, we performed live imaging of wing imaginal discs containing heat shock–induced polyploid clones via a FLP-out mosaic system (Germani et al., 2018). These induced polyploid cells, dispersed throughout the disc, displayed striking morphological features including elongated, dynamic membrane protrusions (Fig. 1, C–F) that extended and retracted over time. These extensions frequently made transient contacts with distant cells or with basal regions of the epithelium (Fig. 1 C; Fig. S1, G–H; and Videos 1, and 2). Notably, many induced polyploid cells appeared to delaminate from the epithelial sheet, traversing to the basal surface and exhibit prominent multidirectional protrusive activity (Videos 1 and 2). In contrast, control clones expressing *lacZ* showed no obvious protrusive activity or centroid displacement (Video 3). During this process, the maximum protrusion length of *fzr-OE* cells reached ∼70 µm, with an average protrusion length of 36.68 µm and an average centroid displacement speed of ∼0.25 µm per minute (Fig. 1, D and E). In *rux-OE* clones, protrusion lengths reached up to 155 µm, with an average length of 97.87 µm and an average centroid displacement speed of ∼0.32 µm per minute (Fig. 1, D and E). In contrast, wing disc cells expressing *fzr RNAi* or *rux RNAi* showed no cellular protrusions or signs of enhanced cell dynamics (Fig. S1, B–D). Similarly, knockdown of *CycB* (*CycB* RNAi) did not induce polyploidy and was not associated with any dynamic cellular behavior (Fig. S1, E and F). In a separate imaging experiment (Video 4), induced polyploid cells were observed navigating around a large tubular structure identified as the trachea. These cells extended protrusions toward or underneath the tracheal tube and tracked along its basal surface, suggesting that the trachea may serve as a physical guide or structural cue for biased displacement. Together, these live-imaging data demonstrate that induced polyploid cells adopt extensive cellular remodeling and dynamic exploratory behavior.

To assess whether polyploidy also contributes to developmental cell migration, we examined border cells in egg chambers, a well-established model of collective migration (Montell, 2003). Border cells are specialized follicle cells that migrate through nurse cells during stage nine of oogenesis (Montell, 2003). Using *C306-Gal4* (Miao et al., 2022), which is expressed in the stalk cells and border cells (Fig. 2 A), we induced expression of *CycE RNAi* or a stabilized form of E2f1 (*E2F1^{PIP3A}*) (Shibutani et al., 2008; Zielke et al., 2011) to reduce ploidy in border cells. Reduced ploidy was confirmed by measuring nuclear size in stage 10 egg chambers. Compared with main-body follicle cells and control border cells (which normally have a ploidy of ∼16C), border cells overexpressed with *CycE RNAi* or *E2f1^{PIP3A}* exhibited significantly reduced nuclear size, corresponding to less than half of the normal ploidy (Fig. 2 C). Importantly, this reduction in ploidy was associated with impaired migratory behavior. Whereas GFP-labeled control border cell clusters reached the oocyte as expected, knockdown of CycE or stabilization of E2f1 resulted in pronounced migration defects, with border cells in some egg chambers failing to reach the oocyte by stage 10 (Fig. 2, B–E). In some cases, border cells also failed to delaminate from the anterior pole by stage 10 (Fig. 2, D and E). These results indicate that polyploidy is required for efficient border cell migration during development.

Together, these findings show that polyploid cells exhibit enhanced dynamic behavior in both experimentally induced wing disc cells and naturally occurring polyploid border cells during development.

Ligand-independent JNK activation is required for polyploidy-induced dynamic behavior

The JNK signaling pathway plays a critical role in both developmental cell migration and tumor cell invasion (La Marca and

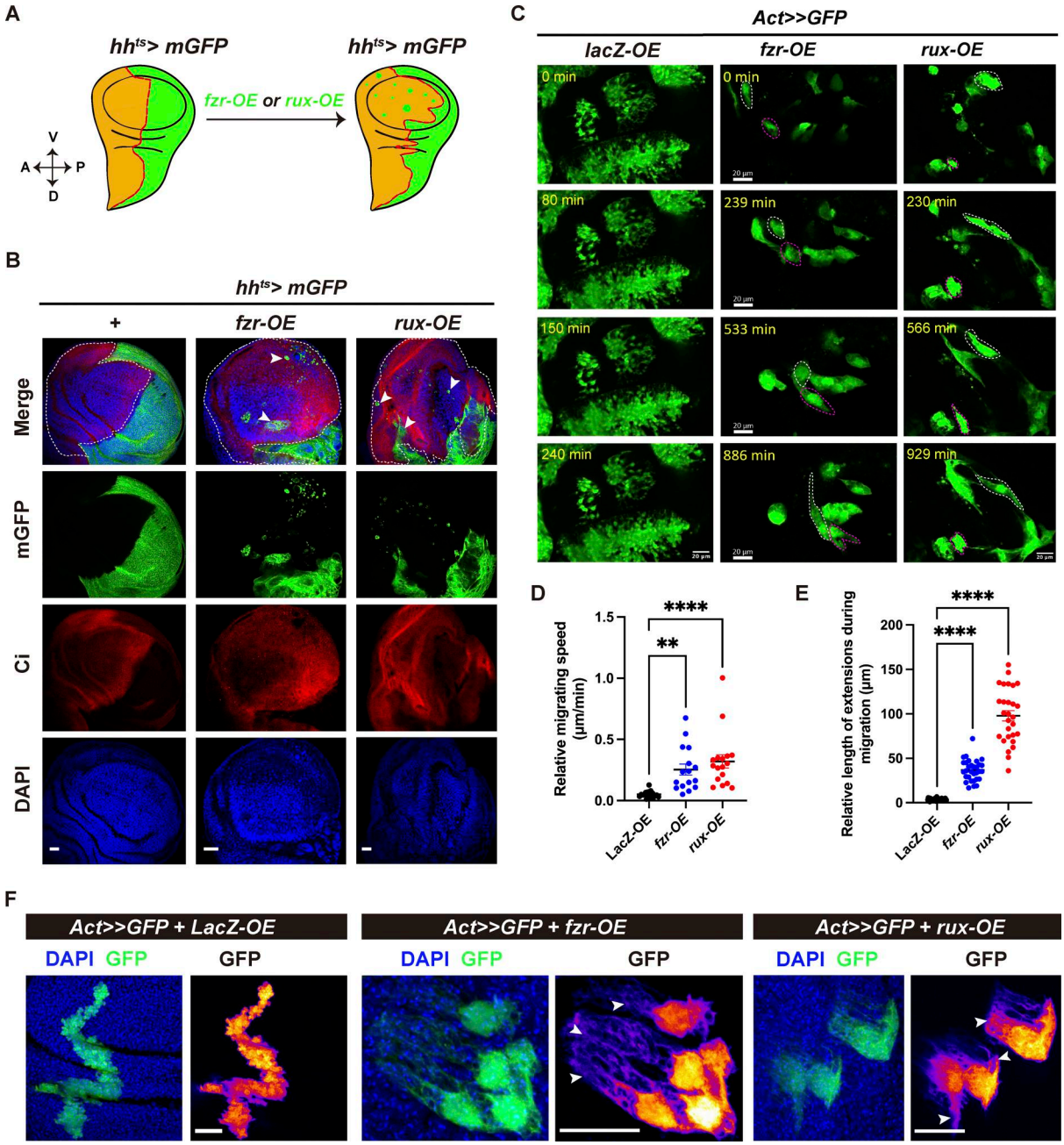

Figure 1. **Induced polyploid cells exhibit dynamic cell behavior in epithelial tissues. (A)** Schematic showing induction of polyploidy via *fzr*-OE or *rux*-OE in the posterior compartment of the wing disc using *hh*^{ts}>Gal4, with subsequent appearance of cells in the anterior compartment. **(B)** Representative confocal images of wing imaginal discs expressing *fzr*-OE or *rux*-OE under *hh*^{ts}>Gal4, compared with control (+). Discs were stained for Ci (red) to mark the anterior compartment and DAPI (blue) to label nuclei. mGFP (green) marks the expression domain. White arrows indicate cells detected in the anterior compartment. **(C)** Time-lapse images of wing disc and discs expressing *lacZ*-OE, *fzr*-OE, or *rux*-OE clones (green) using *Act>>GFP*. White and magenta dashed regions indicate *fzr*-OE or *rux*-OE clones showing dynamic displacement overtime. **(D)** Quantification of relative centroid displacement speed (distance [μm] per minute) for *lacZ-OE* (n = 18), *fzr-OE* (n = 16), and *rux-OE* (n = 17) clones. **(E)** Quantification of maximum protrusion length of *lacZ*-OE (n = 38), *fzr*-OE (n = 31), and *rux*-OE (n = 28) clones during dynamic protrusive activity. **(F)** Confocal images of *lacZ*-OE, *fzr*-OE, and *rux*-OE clones generated by *Act>>GFP*, showing diverse morphologies and evidence of protrusive activity. GFP (green, LUT) marks clone cells; DAPI (blue) marks nuclei. White arrows indicate protrusions. Data are mean ± SEM and were analyzed by one-way ANOVA across three groups. **** represents P value ≤ 0.0001; ** represents P value = 0.0016. Scale bars: 20 μm.

Richardson, 2020). Previous studies have reported JNK activation in wing disc cells undergoing unscheduled polyploidy (Huang et al., 2024). To determine whether JNK mediates the dynamic behavior of polyploid cells, we first examined its activity in border cells using TRE-RFP, a transcriptional reporter (Chatterjee and Bohmann, 2012). TRE-RFP was robustly expressed in migrating border cells (Fig. S2 A), consistent with earlier findings that JNK regulates cell–cell and cell–substratum interactions during collective migration (Llense and Martín-Blanco, 2008).

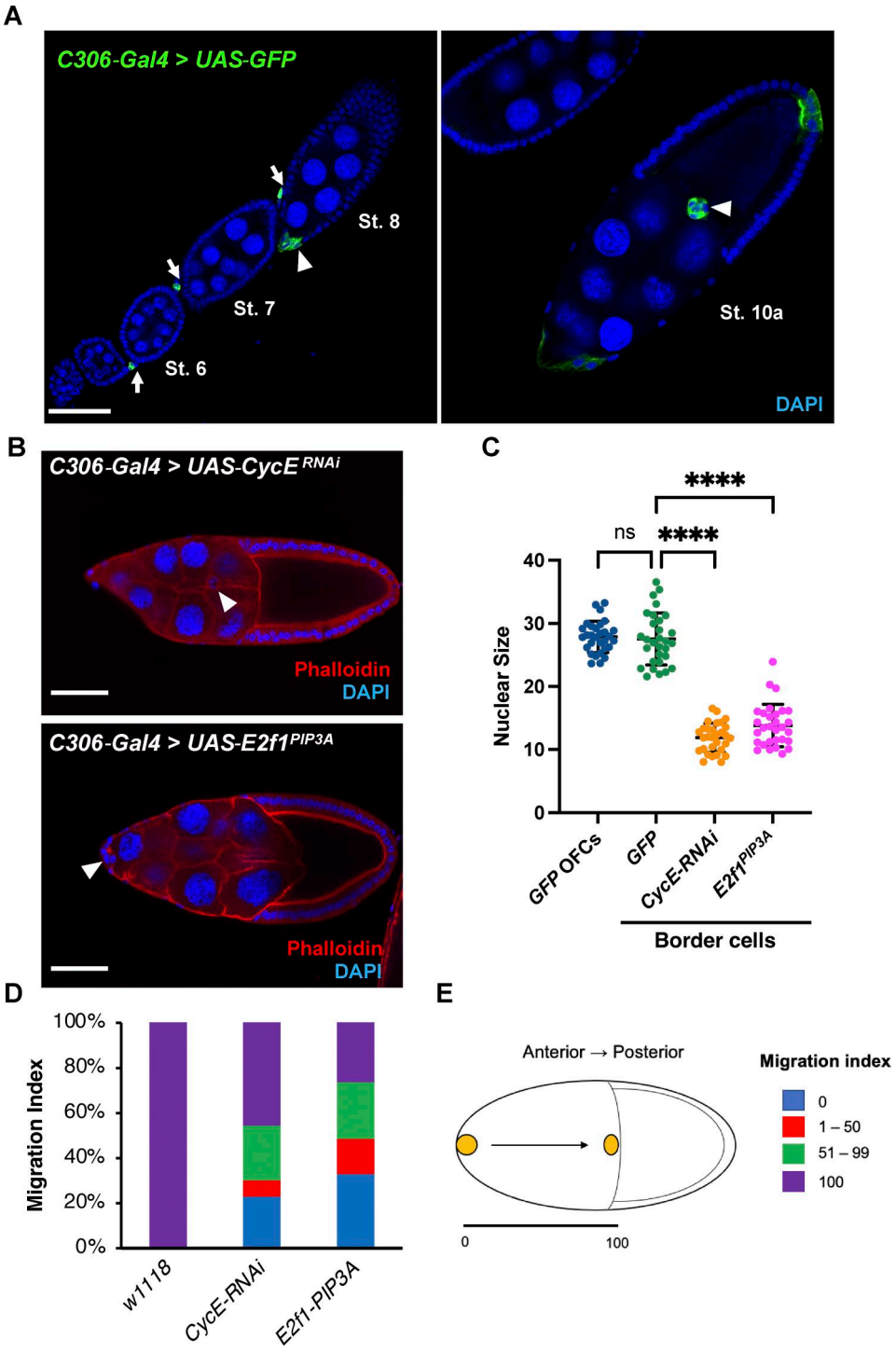

Figure 2. **Polyploidy is essential for border cell migration. (A)** Egg chambers from *c306-Gal4>UAS-GFP* ovary. The *C306-Gal4* is specifically expressed in the stalk cells (arrows) and the border cells (arrowheads). Nuclei are labeled with DAPI (blue). **(B)** Stage 10a egg chambers expressing *CycE-RNAi* in border cells cluster (upper panel) or *E2f1*^{PIP3A} (a stable and active form of E2f1) in the border cell cluster (lower panel). F-actin is stained with phalloidin (red) and nuclei with DAPI (blue). **(C)** Quantification of border cell ploidy in the stage 10 egg chambers. Nuclear area was measured from z-stack confocal images using the central cross section (the largest image) of each nucleus. The left two quantitative data in the graph show the results of oocyte follicle cells (OFCs) and border cells from stage 10 egg chambers expressing only GFP in border cells. In stage 10 egg chambers, all follicle cells should have completed three rounds of endoreplication, corresponding to ~16C ploidy. Compared with these controls, border cells expressing *CycE-RNAi* or *E2f1*^{PIP3A} show nuclear areas less than half of control, indicating they lack one or two rounds of endoreplication compared with normal 16C ploidy cells. **** represents $P < 0.001$ (unpaired two-tailed Student's *t* test); $n = 30$ cells from six egg chambers from *c306-Gal4>UAS-GFP* (*GFP* OFCs and *GFP*), *c306-Gal4>UAS-CycE-RNAi*, and *c306-Gal4>UAS-E2f1*^{PIP3A} ovaries. **(D)** Quantification of border cell migration in the egg chambers from *c306-Gal4* ($n = 47$), *c306-Gal4>UAS-CycE-RNAi* ($n = 70$), and *c306-Gal4>UAS-E2f1*^{PIP3A} ($n = 107$) ovaries. **(E)** A schematic diagram of the border cell migration index. Scale bars, 50 µm.

Next, we assessed JNK activity in polyploid cells induced in the wing disc by overexpressing *fzr* or *rux*. Staining for matrix metalloproteinase 1 (Mmp1), a key JNK target and ECM-degrading protease (Herrera and Bach, 2021), revealed strong upregulation in polyploid cells compared with surrounding diploid tissues (Fig. 3 A). To further validate JNK activation, we examined TRE-RFP expression in both fixed and live samples and found that it was prominently expressed in polyploid *fzr-OE* and *rux-OE* cells. Specifically, ∼75.78% of *fzr-OE* clones (231 clones from 16 discs) and ∼75.76% of *rux-OE* clones (108 clones from 11 discs) exhibited strong TRE-RFP signals (Fig. 3, B–D; Fig. S2, B and C; and Videos 5 and 6), confirming elevated JNK activity.

To determine whether JNK activation is required for these behaviors, we expressed a dominant-negative form of the Jun kinase basket (bsk^{DN}) (Weber et al., 2000). Inhibition of JNK signaling significantly reduced Mmp1 expression and AP boundary-crossing behavior. Only ∼40.74% (n = 27) of *fzr-OE* + bsk^{DN} discs and ∼35% (n = 40) of *rux-OE* + bsk^{DN} discs showed cells crossing the AP boundary, compared with nearly 100% of control discs (*fzr-OE*, n = 25; *rux-OE*, n = 29) (Fig. 4). These results indicate that JNK signaling is essential for polyploid cell dynamic behavior.

In *Drosophila*, JNK signaling is typically activated by the TNF superfamily ligand Eiger, which signals through the receptors Grindelwald (Grnd) or Wengen (Wgn), initiating a kinase cascade involving Msn (JNKKKK), dTAK1 (JNKKK), Hep (JNKK), and Bsk (JNK) (Herrera and Bach, 2021). To test whether JNK activation in polyploid cells is ligand dependent, we inhibited upstream signaling by expressing a dominant-negative form of *grnd* ($grnd^{DN}$ [Andersen et al., 2015]) or RNAi against *wgn* (*wgn-RNAi* [de Vreede et al., 2018; Wang et al., 2024]). Strikingly, blocking either receptor had minimal impact on cell dynamics or Mmp1 expression in polyploid cells (Fig. 4; and Fig. S2, D and E). Approximately 90% of *fzr-OE* (n = 19) or *rux-OE* (n = 20) polyploid cells expressing $grnd^{DN}$, and over 94% of those expressing *wgn-RNAi* (*fzr-OE*, n = 17; *rux-OE*, n = 8), still exhibited robust AP boundary-crossing behavior (Fig. 4; and Fig. S2, D and E). These findings suggest that JNK activation in polyploid cells occurs independently of the canonical TNF ligand-receptor signaling. Although these results argue against a requirement for Grnd- or Wgn-mediated signaling, they do not exclude all forms of non–cell-autonomous regulation of JNK activation.

Together, these results show that JNK signaling is both activated and required for polyploid cell dynamics. The ligand-independent nature of this activation points to intrinsic cellular stress, rather than external cues, as the primary driver of JNK-mediated motility-like behavior in polyploid cells.

Elevated ROS drives JNK activation in polyploid cells

Polyploid cancer cells are known to exhibit higher levels of ROS than their diploid counterparts (Roh et al., 2012). ROS can activate signaling pathways such as JNK and have been implicated in promoting tumor progression, while antioxidants suppress JNK activity (Fogarty et al., 2016; Garcia-Arias et al., 2023; Pinal et al., 2018; Santabárbara-Ruiz et al., 2015). Given the requirement of JNK signaling for polyploid cell dynamic behavior, we tested whether elevated ROS contributes to JNK activation in polyploid cells.

To assess ROS levels, we used GstD-GFP, a reporter for oxidative stress in *Drosophila* (Sykiotis and Bohmann, 2008). Polyploid cells generated by *fzr-OE* or *rux-OE*, driven by cubitus interruptus (*Ci*)-*Gal4* (Tripathi et al., 2022) with a tub-Gal80^{ts} to provide temporal control of gene expression (Ci^{ts}>*Gal4*), showed a significant increase in GstD-GFP fluorescence compared with neighboring diploid cells (Fig. 5 A), indicating elevated ROS production in polyploid cells. This suggested that polyploidy is associated with heightened oxidative state, which could be driving JNK activation and motility-like behavior.

To test whether ROS production is required for JNK activation in polyploid cells, we overexpressed the antioxidant enzymes catalase (*Cat*) or superoxide dismutase 1 (*Sod1*), both of which reduce intracellular ROS levels (Thannickal and Fanburg, 2000). As expected, overexpression of either *Cat* or *Sod1* in *fzr-OE* polyploid cells significantly decreased GstD-GFP levels (Fig. S3, A and C). Importantly, both the JNK reporter TRE-RFP and the JNK target Mmp1 showed reduced expression upon antioxidant overexpression (Fig. 5, B and D; and Fig. S3, E and G). A similar trend was also observed in *rux-OE* polyploid cells: overexpression of either *Cat* or *Sod1* significantly reduced GstD-GFP levels (Fig. S3, B and D), and JNK activity was also decreased following antioxidant overexpression (Fig. 5, C and E; and Fig. S3, F and H). Consistent with these findings, overexpression of *sod1* or *cat* partially inhibited the dynamic behavior of *fzr-OE* or *rux-OE* cells. Specifically, in the *fzr-OE + sod1-OE* group, 35.71% of discs (5/14) showed no AP boundary-crossing events, whereas 58.33% of discs (7/12) lacked such events in the *fzr-OE + cat-OE* group. Similarly, in the *rux-OE + sod1-OE* group, 28.57% of discs (4/14) showed no *rux-OE* boundary-crossing evens, and 48.38% of discs (15/31) showed on migration-like behavior in the *rux-OE + cat-OE* group. These results indicate that elevated oxidative stress promotes JNK activation, which partially contributes to induced polyploid cell dynamic behavior in this context.

To further validate the role of ROS, we treated larvae with N-acetyl cysteine (NAC), a widely used ROS scavenger, and monitored ROS and JNK activity (Aldini et al., 2018; Shields et al., 2021). NAC-fed larvae exhibited a substantial reduction in GstD-GFP signal, confirming lower ROS levels (Fig. S3, I and J). Correspondingly, Mmp1 expression was markedly reduced in polyploid cells from NAC-treated discs compared with untreated controls (Fig. S3, I and K). These results collectively support the conclusion that elevated ROS production is a key upstream signal that drives JNK activation in polyploid cells, promoting their motility-associated dynamic behavior.

Polyploidy-associated ER stress is a key driver of dynamic polyploid cell behavior

ER stress is a widely accepted source of ROS and is often triggered by the accumulation of unfolded or misfolded proteins in the ER, initiating the unfolded protein response (UPR) (Chen et al., 2023). Given the elevated metabolic and biosynthetic activity typically associated with polyploidy, we hypothesized that polyploid cells might experience higher levels of ER stress.

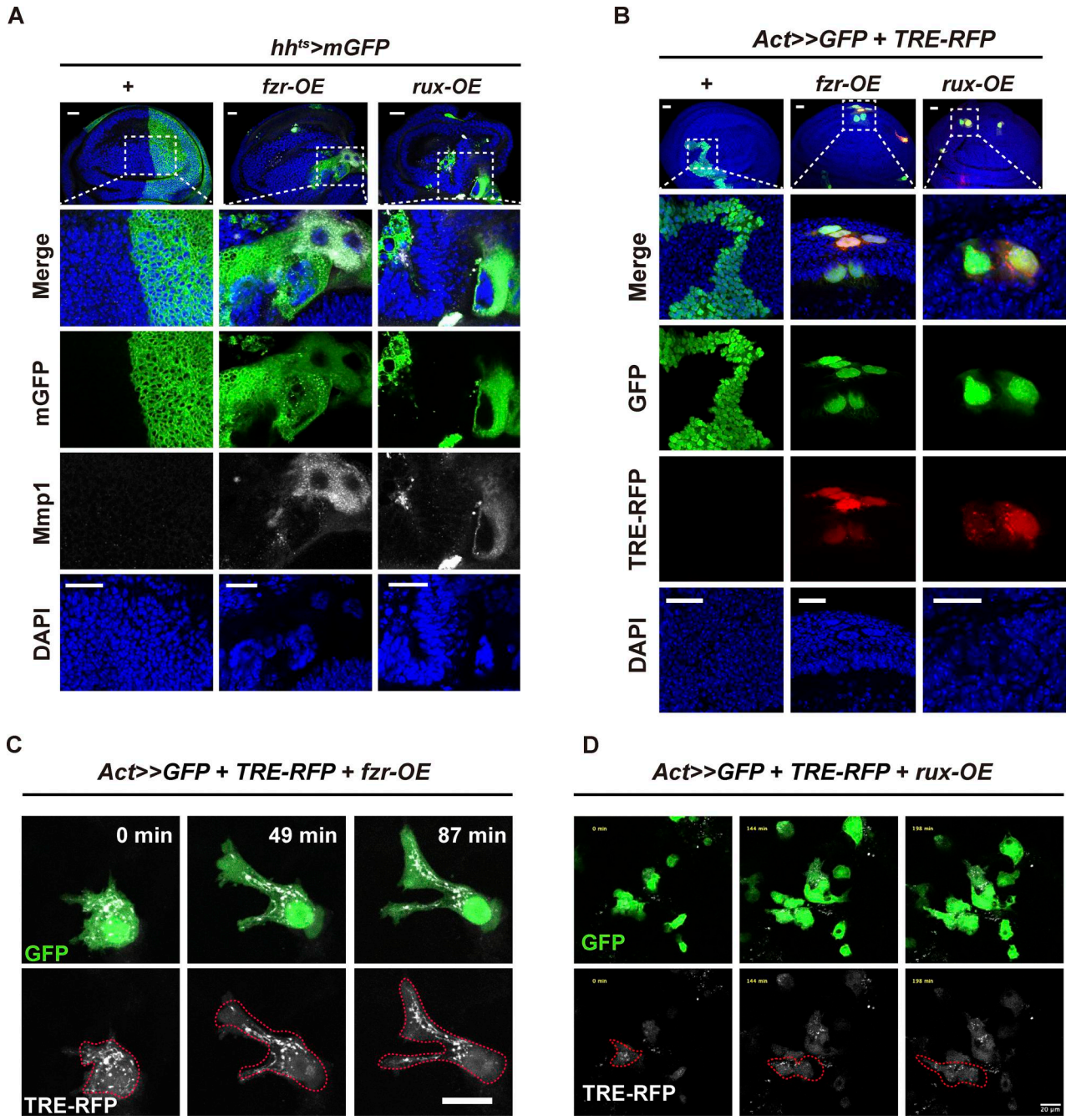

Figure 3. **JNK signaling is activated in induced polyploid cells. (A)** Representative confocal images of wing discs expressing *fzr*-OE or *rux*-OE under *hh*>Gal4, compared with control (+). Discs were stained for Mmp1 (gray) and DAPI (blue) and expressed membrane GFP (mGFP, green). White dashed boxes in the top panels highlight regions shown in the magnified images below. **(B)** Confocal images of FLP-out clones expressing *fzr*-OE or *rux*-OE under *Act>>GFP* control. TRE-RFP (red) reports JNK pathway activity; GFP marks clones (green), and DAPI (blue) marks nuclei. White dashed boxes in the top panels highlight regions shown in the magnified images below. **(C)** Time-lapse imaging of an *Act>>GFP* + *fzr*-OE clone (GFP, green) expressing TRE-RFP (gray). Red dashed regions mark TRE-RFP patterns, showing dynamic JNK activation over time. **(D)** Time-lapse imaging of an *Act>>GFP* + *rux*-OE clone (GFP, green) expressing TRE-RFP (gray). Red dashed regions mark TRE-RFP pattern, showing dynamic JNK activation over time. Scale bars: 20 µm.

Consistent with this idea, we observed a significant increase in protein synthesis in polyploid cells driven by *pdm2-gal4* (which is primarily expressed in the wing pouch and also in the outer edge of the distal hinge region [Huang et al., 2024; Loker and Mann, 2022]) compared with diploid cells, as detected by the O-propargyl-puromycin (OPP) protein synthesis assay (Fig. 6, A and B), suggesting heightened ER activity. To directly assess ER stress, we used an ER stress reporter line (Xbp1-dsRed), which fluoresces upon splicing of *Xbp1* mRNA, a hallmark of UPR activation (Bergmann et al., 2013). Strong Xbp1-dsRed signals were detected in polyploid cells, with 92.01% of *fzr-OE* clones (n = 158) and 94.68% of *rux-OE* clones (n = 148) showing

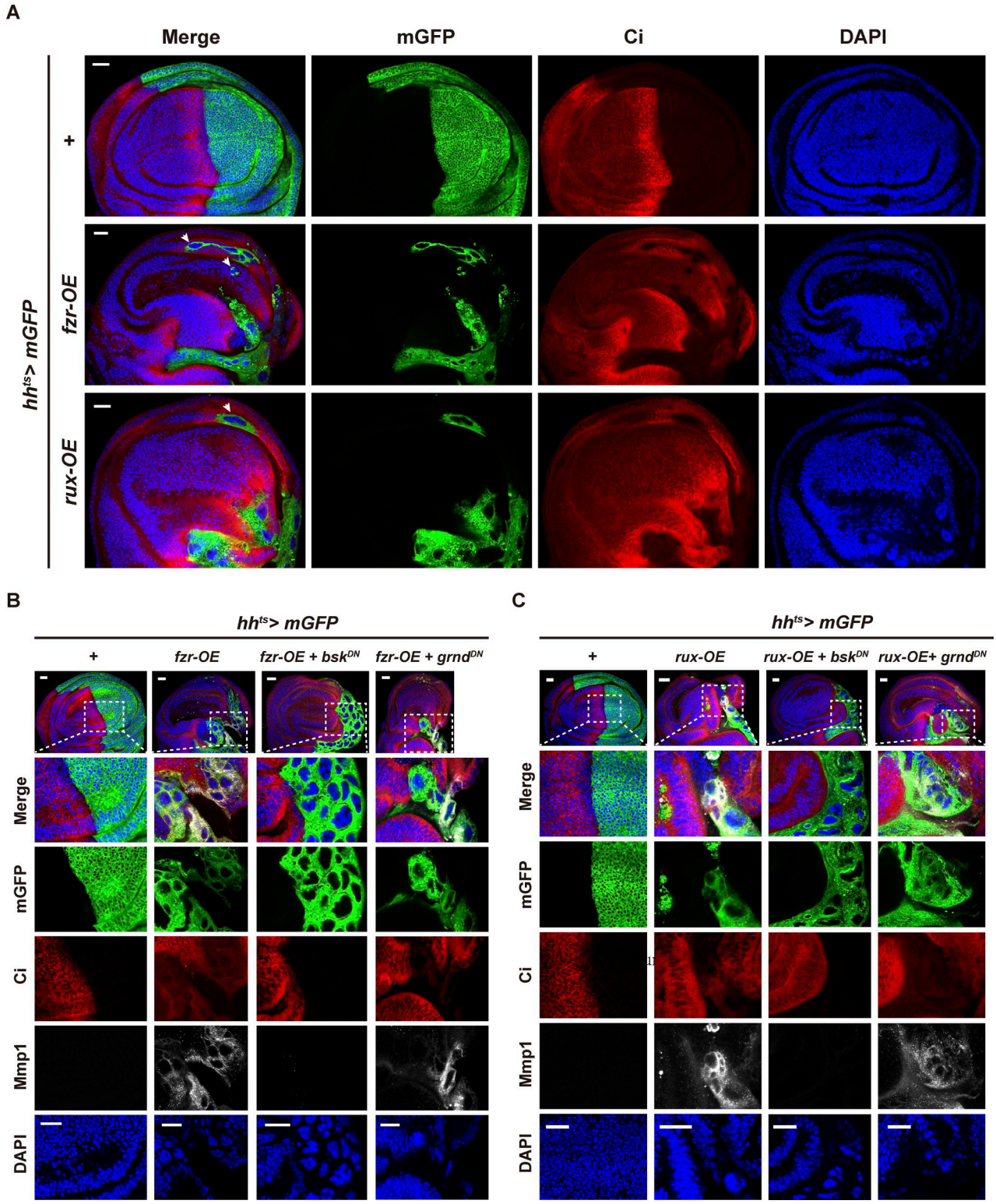

Figure 4. **JNK signaling is required for induced polyploid cell dynamics. (A)** Representative confocal images of wing discs expressing *fzr*-OE or *rux*-OE under *hh*>Gal4, compared with the control (+). Clones are marked by mGFP (green). Discs were stained with Ci (red) and DAPI (blue). White arrowheads indicate polyploid cells that have crossed into the anterior compartment. **(B)** Representative confocal images of wing discs expressing *fzr*-OE alone or in combination with bsk^{DN} or $grnd^{DN}$, compared with control (+). Discs were stained for Mmp1 (gray), Ci (red), and DAPI (blue), with mGFP (green) marking the posterior compartment. **(C)** Representative images of *rux*-OE wing discs, with or without co-expression of bsk^{DN} or $grnd^{DN}$, compared with control (+), stained as in B. In both A and B, white dashed rectangles in the top panels highlight regions shown in the magnified images below. Scale bars: 20 µm.

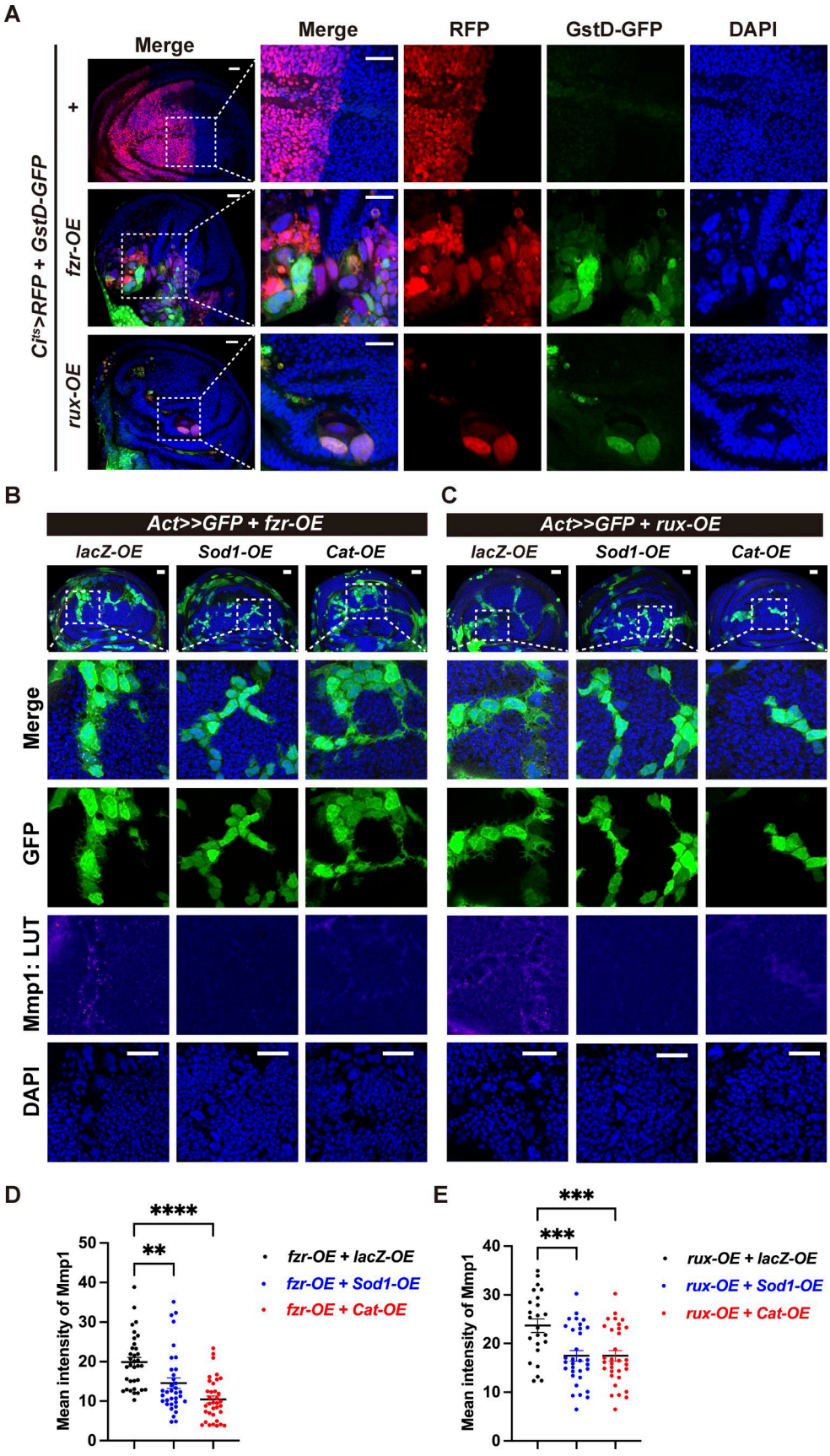

Figure 5. **JNK activation in induced polyploid cells is triggered by ROS. (A)** Representative confocal images showing the expression of the oxidative stress reporter *GstD-GFP* (green) in control (+), *fzr*-OE, and *rux*-OE wing discs. RFP marks the expression domain (red), and DAPI stains nuclei (blue). Magnified views of

the boxed regions (white dashed rectangles) are shown in subsequent columns. **(B)** Confocal images of wing discs with *fzr*-OE clones co-expressing *lacZ*-OE, *Sod1*-OE, or *Cat*-OE (GFP, green). Discs were stained with Mmp1 (gray) as a readout of JNK activity and DAPI (blue) to label nuclei. **(C)** Confocal images of wing discs with *rux*-OE clones co-expressing *lacZ*-OE, *Sod1*-OE, or *Cat*-OE (GFP, green). Tissues were stained with Mmp1 (gray) for JNK activity and DAPI (blue) for nuclei. In B and C, the top row shows whole discs; lower panels show magnified views of boxed regions. **(D)** Quantification of Mmp1 signal intensity in clones from *fzr-OE + lacZ-OE* (n = 34), *fzr-OE + sod1-OE* (n = 35), or *fzr-OE + cat-OE* (n = 35). **(E)** Quantification of Mmp1 signal intensity in clones from *rux-OE + lacZ-OE* (n = 24), *rux-OE + sod1-OE* (n = 32), or *rux-OE + cat-OE* (n = 32). Data are mean ± SEM analyzed by one-way ANOVA in three groups. **** represents P value ≤0.0001, *** represents P value = 0.0008, and ** represents P value = 0.0028. Scale bars: 20 µm.

reporter activation (Fig. 6, C–E). We also used KDEL-RFP (Milano et al., 2025), an ER marker, to assess ER status in *fzr-OE* and *rux-OE* polyploid cells. Approximately 98% of induced polyploid clones showed a punctate KDEL-RFP signal pattern (Fig. S4, A and B). These results confirm that polyploid cells undergo significant ER stress.

To determine whether ER stress contributes to JNK activation, we overexpressed Xbp1, a key factor that enhances protein folding and ER-associated degradation, thereby alleviating ER stress. To further confirm elevated ROS levels in induced polyploid cells, we used the cell-permeable fluorescent probe dihydroethidium (DHE) to detect ROS (Deng et al., 2018). Consistent with our GstD-GFP reporter results, induced polyploid cells exhibited high DHE signals (Fig. S4 C). Overexpression of Xbp1 in induced polyploid cells reduced the DHE signal, indicating that ROS levels decreased following Xbp1 overexpression (Fig. S4 C). Furthermore, Xbp1 overexpression in *fzr-OE* and *rux-OE* polyploid cells significantly reduced Mmp1 expression (Fig. 6, F–I), indicating diminished JNK activity. Together, these results suggest that alleviating ER stress suppresses the JNK-ROS signaling axis.

Induced polyploid cells exhibit phagocytic activity

Given that induced polyploid cells in epithelial tissues display dynamic, motility-like behavior, we next sought to determine whether this dynamic phenotype is functionally linked to additional cellular activities. One such activity is phagocytosis, which has recently been associated with polyploidy in *Drosophila* follicle epithelial cells. Under stress conditions such as starvation, these polyploid follicle cells adopt a NPP identity, enabling them to engulf and remove apoptotic germline cells as part of a protective tissue response (Huang et al., 2025). This raised the possibility that polyploid cells in other epithelial contexts, such as the imaginal discs, may similarly acquire phagocytic capabilities in response to tissue stress.

To explore this further, we examined whether induced polyploid cells in the imaginal disc could engulf neighboring apoptotic cells. We analyzed *fzr-OE* polyploid cells in the wing disc and *rux-OE* polyploid cells in the eye disc and found that both were capable of internalizing apoptotic debris from adjacent dying cells (Fig. 7, A and B; and Fig. S5, A and B). However, under unstressed conditions, this phagocytic behavior was relatively infrequent, likely due to the low incidence of spontaneous apoptosis in developing tissues.

To test whether phagocytosis is enhanced in response to increased apoptotic burden, we subjected the tissues to γ irradiation, an established method to induce widespread apoptosis (Shinomiya, 2007; Verheij and Bartelink, 2000; Zhang et al., 2014a). At 24 h after irradiation, we observed extensive apoptosis in diploid cells throughout the discs, while polyploid cells remained largely viable, consistent with their known radiation resistance (Wang and Tamori, 2024). Strikingly, under the irradiated stress conditions (18Gy), we detected a significant increase in polyploid cells engulfing neighboring apoptotic neighbors (Fig. 7, C and D; and Fig. S5, C and D). Occasionally, we observed that these polyploid cells also gripped live neighboring cells (Fig. S5, E–H). To determine whether increased engulfment reflects elevated cell death, we quantified cell death events in control, *fzr-OE*, and *rux-OE* wing discs. We found no significant differences in cell death levels among these conditions (Fig. S5, I and J), indicating that enhanced engulfment is not simply a consequence of increased cell death.

These results indicate that polyploid cells not only survive better under genotoxic stress but also actively participate in the clearance of apoptotic cells—functions typically associated with professional phagocytes such as hemocytes or NPPs such as glial cells (Melcarne et al., 2019).

Polyploid cells acquire engulfing ability within tumor tissues

Live-cell engulfment, also referred to as entosis, is frequently observed in human cancer cells (Overholtzer et al., 2007). It has been proposed that entosis can act as cell cannibalism where more aggressive tumor cells outcompete less aggressive ones and that this selects for more invasive, fitter clones, accelerating tumor malignancy (Kroemer and Perfettini, 2014). To investigate whether polyploid cells exhibit phagocytic behavior in tumor environments, we analyzed tumorigenic wing discs from *scrib*^{1}/*scrib*^{j7B3} (scribble, tumor suppressor [Santoni et al., 2020]) trans-heterozygous mutant larvae containing mosaic clones expressing either GFP alone or *fzr* together with GFP. Three days after clone induction, the discs were stained with anti-cleaved Dcp1 (cDcp1) to label apoptotic cells. The mosaic clones expressing only GFP in the tumors did not exhibit phagocytic behaviors, including cellular protrusions or engulfing neighbor cells (Fig. 7 E). In contrast, in discs containing *fzr*-overexpressing polyploid clones, we observed prominent cellular protrusions extending from the polyploid clones (Fig. 7, F and G, indicated by white arrowheads). Notably, neighboring non-polyploid tumor cells (GFP-negative) were frequently found within the *fzr*-expressing clones, suggesting active engulfment.

Following exposure to 35 Gy of γ-ray irradiation 24 h prior to dissection, the engulfment phenotype was further enhanced, with more frequent and pronounced instances of non-polyploid cells being internalized by adjacent polyploid cells (Fig. 7, G–I). DAPI staining confirmed the presence of multiple engulfed nuclei within the polyploid clones. These results demonstrate that *fzr*-induced polyploid cells in tumor tissues can extend cellular

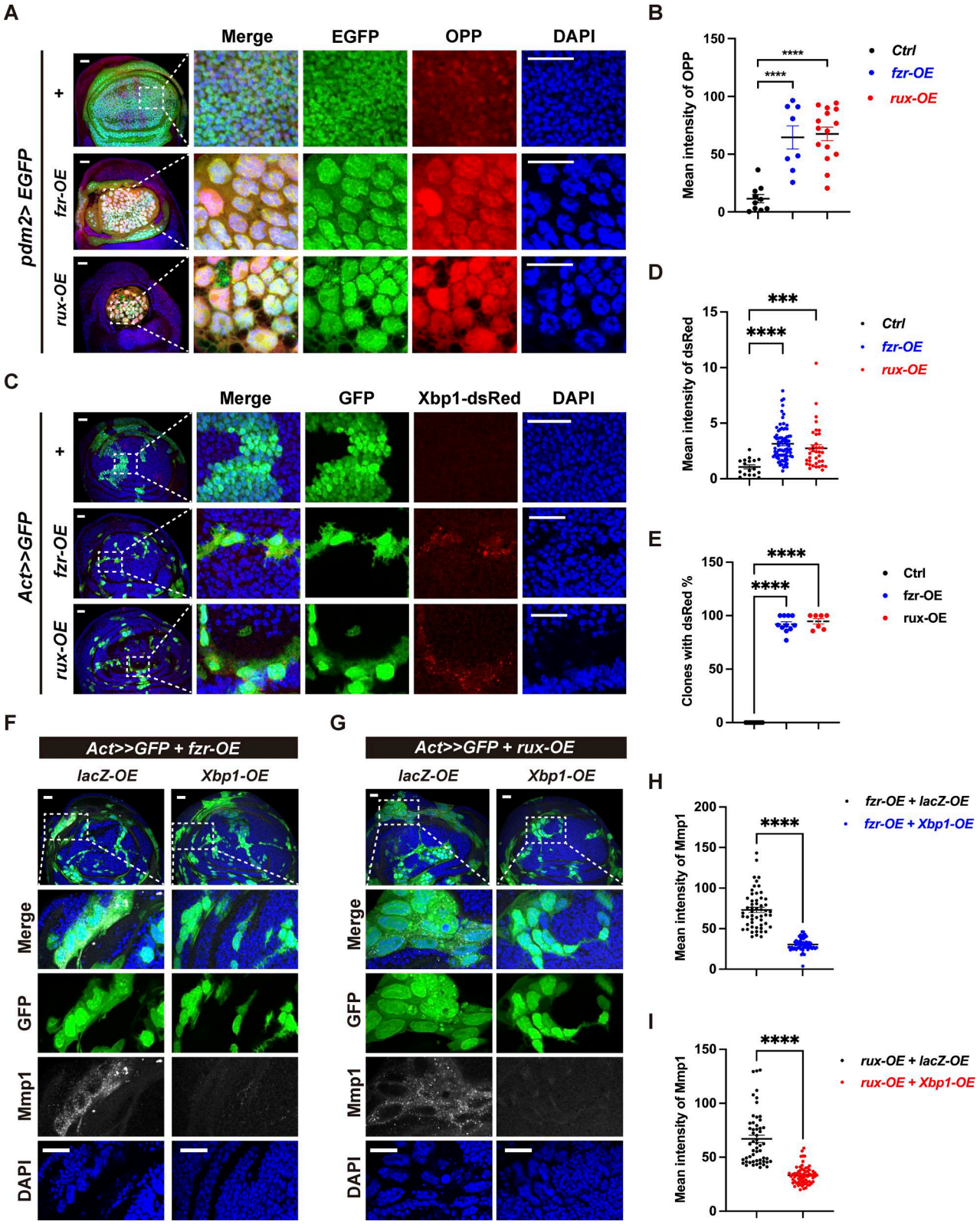

Figure 6. **ER stress is a potential source of ROS in induced polyploid cells. (A)** Representative confocal images of control (+), *fzr-OE*, and *rux-OE* wing discs stained for OPP (red) to label active protein synthesis. EGFP marks expression domains (green), and DAPI stains nuclei (blue). **(B)** Quantification of OPP signal intensity shown in control (n = 10), *fzr-OE* (n = 8), and *rux-OE* (n = 15). **(C)** Expression of the ER stress reporter *Xbp1-dsRed* (red) in control (+), *fzr-OE*, and *rux-OE* clones (GFP, green); DAPI marks nuclei (blue). **(D)** Quantification of *Xbp1-dsRed* signal intensity in control (ctrl) (n = 17), *fzr*-OE (n = 76), and *rux*-OE (n = 37). **(E)** Percentage of control (n = 10), *fzr*-OE (n = 11), and *rux*-OE (n = 7) clones exhibiting strong *Xbp1-dsRed* signal. **(F and G)** Confocal images of wing discs expressing *fzr*-OE (F) or *rux*-OE (G) with *lacZ*-OE or *Xbp1*-OE. Clones are labeled with GFP (green); tissues are stained for Mmp1 (gray) and DAPI (blue). **(H and I)** Quantification of Mmp1 signal intensity in discs shown in F and G, respectively. Data are mean ± SEM analyzed by unpaired Student's t test in two groups and one-way ANOVA in three groups. *** represents P value = 0.0008; **** represents P value ≤0.0001. Scale bars: 20 µm.

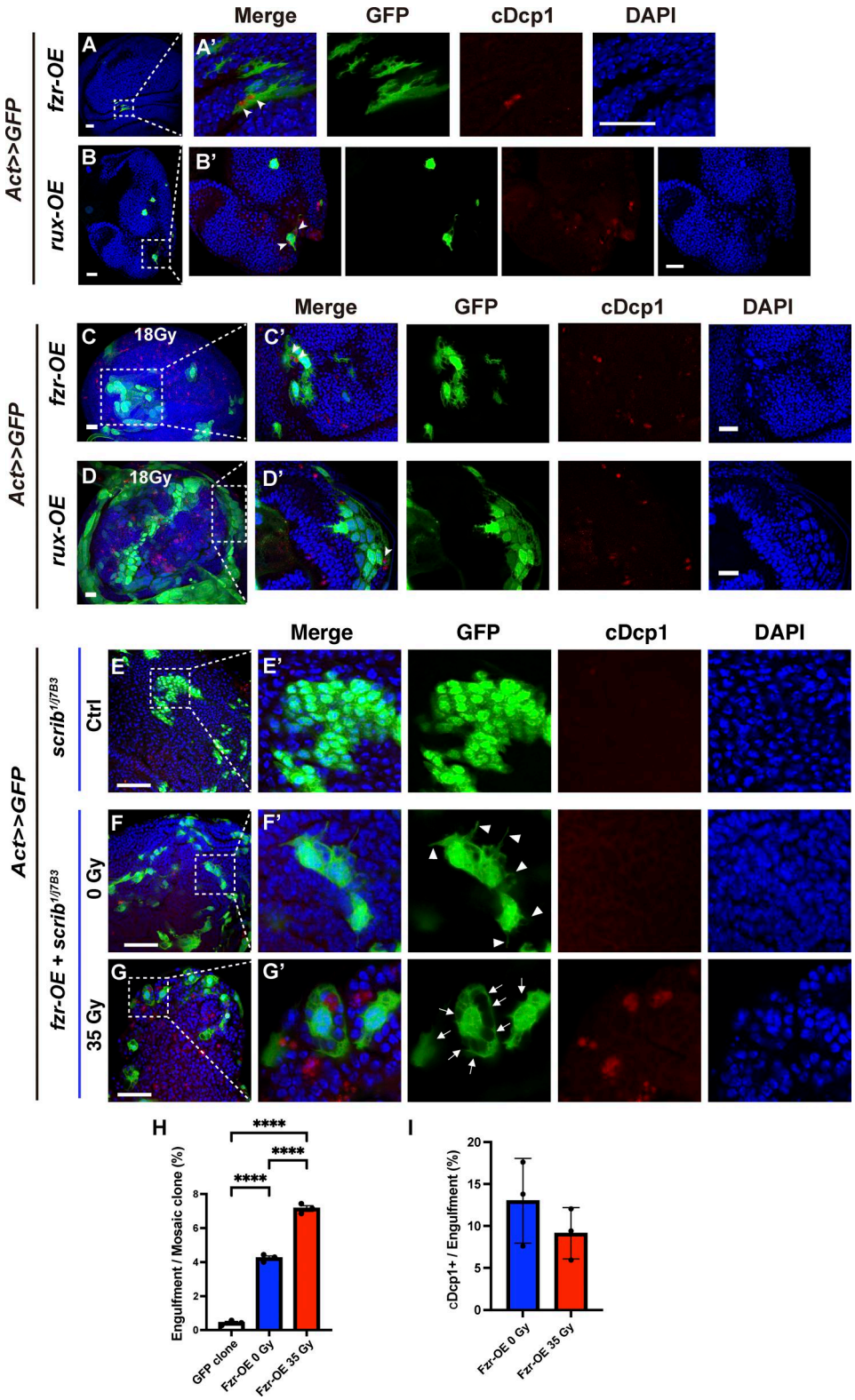

Figure 7. **Induced polyploid cells exhibit engulfment activity. (A and B)** Representative confocal images of *fzr*-OE (A, wing disc) and *rux*-OE (B, eye disc) clones stained for cDcp1 (red) and DAPI (blue). GFP marks polyploid clones (green). Panels A′ and B′ show magnified views of the boxed regions in A and B, respectively. **(C and D)** Confocal images of *fzr*-OE (C) and *rux*-OE (D) clones following exposure to 18 Gy γ-irradiation. Clones were stained with cDcp1 (red) and DAPI (blue); GFP marks polyploid cells (green). Panels C′ and D′ show magnified views of the boxed regions. White arrowheads indicate apoptotic (cDcp1 positive) cells engulfed by neighboring polyploid cells. **(E and G)** Tumorigenic wing discs from *scrib*^{1}/*scrib*^{i7B3} trans-heterozygous mutant larvae containing mosaic GFP-positive clones. **(E and E′)** Control clones expressing GFP only. **(F and F′)** Clones expressing *fzr* (polyploid-inducing) with GFP. **(G and G′)** *fzr*-OE clones in a tumor disc 24 h after 35 Gy γ-irradiation. The second to fifth columns show magnified views of the boxed areas in the first column. cDcp1 (red) marks

apoptotic cells; DAPI (blue) labels nuclei. White arrowheads indicate protrusions from *fzr*-OE polyploid clones; white arrows mark GFP-negative (non-polyploid) tumor cells engulfed by adjacent polyploid cells. **(H)** Quantification of engulfment in $scrib^{1}/scrib^{7B3}$ trans-heterozygous tumorigenic wing discs. The number of GFP-negative cells that are completely engulfed by GFP-expressing mosaic clones was quantified per clone cluster. **(I)** Quantification of apoptotic cells. The number of apoptotic cells (labeled by anti-cDcp1 antibody) per completely engulfed GFP-negative cell within GFP-positive mosaic clones was quantified. Data are mean ± SD from three independent experiments. **** represents $P < 0.001$ (unpaired two-tailed Student's *t* test); $n = 30$ GFP-expressing clones from each indicated experiment. Scale bars: 20 µm (A–D) and 50 µm (E–G).

protrusions and actively engulf neighboring cells, and that this behavior is further augmented by irradiation-induced stress.

To further assess the engulfment behavior of induced polyploid cells, we examined their interactions with less-fit neighboring cells using a cell competition model (Li and Baker, 2007; Nagata and Igaki, 2018; van Neerven and Vermeulen, 2023). Mahjong (*mahj*), a ubiquitin E3 ligase substrate receptor, functions as a well-established "loser" signal in cell competition, leading to selective elimination of *mahj* mutant cells by surrounding cells (Tamori et al., 2010). We performed live imaging of wing discs containing induced polyploid cells at the A/P boundary in a mosaic $mahj^{1}$ mutant background (*hsFlp; 42D hRFP* $mahj^{1}$*/42D ptc>GFP; fzr-OE/+*), which generates a competitive tissue environment. Under these conditions, *fzr-OE* polyploid cells became enlarged, formed prominent cellular extensions, and exhibited strong Mmp1 expression in the presence of $mahj^{1}$ cells (Fig. S5 L). In these recordings, GFP-positive polyploid cells were observed actively engulfing apoptotic $mahj^{1}$ loser cells, providing direct evidence of engulfment behavior (Fig. S5, K and M; and Video 7). Representative frames extracted from these videos, together with fixed-sample confocal imaging, clearly demonstrate internalization of target cells and confirm phagocytic activity by induced polyploid cells (Fig. S5, K–M). Together, these results demonstrate that induced polyploid cells exhibit functional phagocytic behavior, which may contribute to tissue homeostasis and recovery following stress or injury.

Poly-aneuploidy promotes cancer cell migration

Polyploid giant cancer cell, also referred to as poly-aneuploid cancer cell (PACC), contribute to intratumoral heterogeneity and malignancy and have been observed across multiple cancer types (Bukkuri et al., 2023; Moein et al., 2020; Zhang et al., 2014b). To determine whether increased ploidy levels regulate the migratory behavior of mammalian cancer cells, we treated the lung cancer cell lines H1299 and H441 with paclitaxel, a mitotic inhibitor that could induce multinucleation (Giannakakou et al., 2001; Moein et al., 2020). Confocal imaging revealed that paclitaxel-treated cells displayed markedly enlarged nuclei compared with their parental counterparts (Fig. 8, A and B). Quantification of nuclear number further confirmed increased DNA content and ploidy levels following paclitaxel treatment (Fig. 8 C).

We next assessed the migratory capacity of these cells using a Boyden chamber assay. Compared with parental cells, induced poly-aneuploid H1299 and H441 cells showed significantly enhanced migration (Fig. 8 D). Western blot analysis demonstrated that levels of phosphorylated JNK (pJNK) were elevated in poly-aneuploid cells relative to parental cells, while total JNK levels remained comparable (Fig. 8 E), suggesting that JNK activation is associated with increased ploidy levels.

To test whether JNK activity is required for the enhanced migration of poly-aneuploid cells, poly-aneuploid H1299 cells were treated with either the antioxidant NAC or the JNK inhibitor SP600125 (Alkafaas et al., 2024). Both treatments reduced pJNK levels without affecting total JNK protein (Fig. 8 F). Importantly, Boyden chamber assays showed that inhibition of JNK signaling, either by NAC or SP600125, significantly impaired the migration of poly-aneuploid cells (Fig. 8 G).

Together, these results indicate that ROS–JNK signaling is activated in PACCs and is necessary for their enhanced migratory behavior. These findings support the idea that mechanisms linking increased ploidy to cell motility-related behaviors are conserved between *Drosophila* and mammalian systems.

Discussion

This study uncovers a previously underappreciated role for induced polyploidy in promoting dynamic, immune cell–like behaviors, particularly motility-associated activity and phagocytosis, through intrinsic stress signaling pathways. Polyploidy is well recognized for its association with stress resistance and its role in supporting tissue growth or repair (Darmasaputra et al., 2024; Moein et al., 2020). Our findings expand this view by showing that induced polyploid cells are not only stress resistant but also actively responsive, engaging in behaviors typically associated with immune or invasive cells.

These results add to growing evidence that polyploidy plays an active role in tissue remodeling. For example, during zebrafish heart regeneration, polyploid cells function as leader cells, exhibiting enhanced migratory speed and mechanical force (Cao et al., 2017). Similarly, our findings in *Drosophila* demonstrate that polyploidy promotes developmental migration, supporting the idea that increased ploidy can activate intrinsic programs that enhance motility. The connection between increased ploidy and JNK-dependent cell motility suggests that polyploidy may pose an internal stress that activates or enhances motility-related programs in response to physiological or pathological cues.

Interestingly, we found that induced polyploid cells also exhibit phagocytic behavior. Because these cells display hemocyte-like functions, we stained for NimC1 (Kurucz et al., 2007), a hemocyte marker, to distinguish *fzr-OE* polyploid cells from hemocytes. The induced polyploid cells showed staining patterns distinct from those of hemocytes (Fig. S5 N), demonstrating that these cells are not hemocytes. Consistent with this finding, we recently showed that polyploidy enables follicle cells to transition into NPPs capable of engulfing dying germline cells (Huang et al., 2025). Notably, phagocytic behavior in this context is also associated with active JNK signaling (Huang et al., 2025). Similarly, previous studies have reported phagocytic

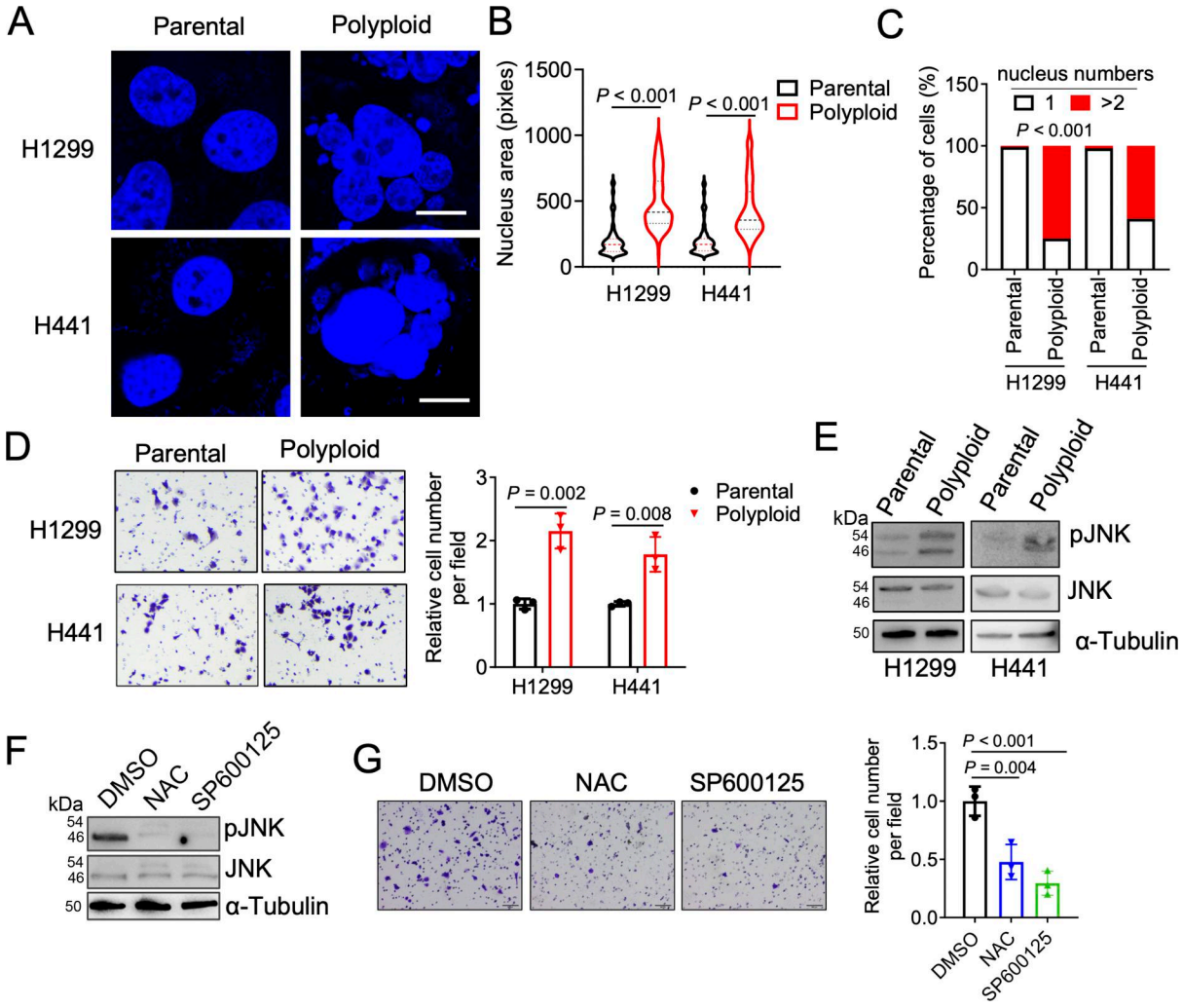

Figure 8. **JNK signaling is required for the migration of induced poly-aneuploid mammalian cells. (A)** Confocal micrographs showing the nuclei of parental and paclitaxel-induced polyploid H1299 and H441 cells. Scale bars: 10 µm. **(B)** Nuclear area in indicated groups. *n* = 100. **(C)** Percentage of cells with one or more nuclei. *n* = 100. **(D)** Boyden chamber migration assay of cells from B; migrated cells were imaged and quantified (graph shown). **(E and F)** Western blot analysis of pJNK and total JNK levels in parental and polyploid cells (E) or in polyploid H1299 cells treated with NAC or the JNK inhibitor SP600125 (F). **(G)** Boyden chamber migration assay of cells from F; migrated cells were imaged and quantified (graph shown). Cells were treated with 1 mM NAC (HY-B0215; MedChemExpress) or 5 µM SP600125 (S1460; selleckchem) for 8 h before functional assays. Source data are available for this figure: SourceData F8.

activity of polyploid tumor cells in *Drosophila* wing discs (Eichenlaub et al., 2016).

Notably, although polyploid cells are present in many tissues, including *Drosophila* salivary gland cells, fat body cells, main follicle cells, and nurse cells, not all polyploid cells are capable of migration. This heterogeneity suggests that polyploidy alone is insufficient to confer motility. Instead, the inability of many polyploid cells to migrate likely reflects the absence of key migratory features, such as actin-based motility machinery, appropriate directional guidance cues, and a permissive tissue environment. Consistent with this view, even within the wing disc, where polyploidy can be experimentally induced, only a subset of polyploid cells exhibits motility-associated behavior (Fig. 2 B and Fig. 4 A), indicating that additional contextual factors are required.

Building on this observation, one critical determinant of migratory competence may be the degree of polyploidy itself, which interacts with local microenvironmental conditions. Induced polyploid cells in the wing disc, as well as migrating border cells, typically undergo a limited number of endoreplication cycles and may therefore retain sufficient cytoskeletal flexibility and regulatory capacity for dynamic remodeling. In contrast, cells with extremely high DNA content, such as nurse cells or polytene salivary gland cells, are likely mechanically constrained, limiting their ability to reorganize the cytoskeleton and respond to migratory cues. Together, these findings suggest that motility of polyploid cells arises from a combination of moderate increases in ploidy and a supportive tissue context, rather than from polyploidy per se.

In addition, we noted that the JNK activity, as indicated by TRE-RFP levels, shows variability among these induced polyploid cells. Induced polyploid cells often exhibit higher *TRE-RFP* levels in the hinge region, where cells are more prone to dynamic behavior. The tumor hotspots also appear in this region, where

tumorigenesis occurs (Tamori et al., 2016). This variability likely reflects differences in cell state and spatial context.

We identify elevated ROS as a key upstream signal that activates JNK in polyploid cells. Both *fzr*- and *rux*-induced polyploid cells exhibited significantly higher oxidative stress, as evidenced by increased GstD-GFP reporter activity. Suppressing ROS levels through overexpression of antioxidant enzymes (*Cat* or *Sod1*) or treatment with the ROS scavenger NAC markedly reduced JNK activity and impaired polyploid cell dynamics. These results suggest that ROS are not merely a byproduct of polyploidy but serve as functional second messengers that drive stress-responsive signaling.

One major source of ROS appears to be ER stress, likely resulting from increased protein synthesis demands of polyploid cells. We observed elevated protein translation and strong activation of the ER stress reporter Xbp1-dsRed, indicating engagement of the UPR (Bergmann et al., 2013). Overexpression of *Xbp1*, which alleviates ER stress by enhancing protein-folding capacity and ER-associated degradation, led to reduced Mmp1 expression in polyploid cells—further supporting the link between ER stress, ROS production, and JNK activation. Importantly, this activation appears to be ligand independent. Blocking canonical JNK pathway receptors had little effect on JNK activity or polyploid cell dynamics, indicating that intrinsic stress, not external cues, drives JNK-mediated behavioral transformation in polyploid cells. This ligand-independent activation highlights a self-contained mechanism by which polyploid cells detect and respond to internal stress, reprogramming themselves to adopt invasive and phagocytic behaviors.

This stress-adaptive mechanism may help explain how polyploid cells gain a selective advantage under adverse conditions, such as nutrient deprivation, oxidative damage, or within the tumor microenvironment. By linking increased ploidy to stress sensing and effector pathways, our findings suggest that polyploid cells act not only as survivors but also as active responders that remodel tissues or evade damage.

These findings have implications for cancer biology, where polyploid and poly-aneuploid cells are often enriched in aggressive, therapy-resistant tumors. Tetraploid colon carcinoma cells exhibit enhanced motility and invasiveness compared with their diploid counterparts (Jemaà et al., 2023), and our data suggest that elevated ROS and JNK activation may underlie these behaviors. Thus, targeting stress-sensing pathways in polyploid cells could represent a therapeutic strategy to limit tumor invasion or promote regenerative healing.

In summary, our study reveals a mechanistic link between polyploidy, intrinsic cellular stress, and adaptive behavior, positioning induced polyploidy as a functional driver of epithelial plasticity across development, regeneration, and disease.

Materials and methods

Fly strains and genetics

Drosophila stocks used in this study are listed in the table below (Table 1). Flies are raised on BDSC standard cornmeal food unless otherwise specified. We note that all experiments were performed in parallel under identical conditions, ensuring that all discs were exposed to the same temperature-shift environment.

Table 1. **Fly strains and genetics**

Stocks	Sources
Act > y⁺>GFP	Lab tool
C306-Gal4	#3743; BDSC
TRE-RFP	Gift from D. Bohmann (University of Rochester Medical Center, Rochester, NY, USA)
UAS rux	#9166, #83155; BDSC
UAS fzr	#91688, #91689; BDSC
UAS rux RNAi	#32467; BDSC
UAS CycB RNAi	#34544; BDSC
UAS fzr RNAi	Gift from D. Fox (#25550; VDRC, Duke University, Durham, NC, USA)
hh^{ts} > CD8GFP	Lab tool
UAS bsk^{DN}	Gift from D. Bilder (University of California, Berkeley, CA, USA)
UAS grnd^{DN}	Gift from D. Bilder (University of California, Berkeley, CA, USA)
UAS wgn RNAi	#58994; BDSC
UAS cycE RNAi	#110204; VDRC
GstD-GFP	Gift from D. Bohmann (University of Rochester Medical Center, Rochester, NY, USA)
Ci^{ts} > RFP	Lab tool
Slbo > GFP	Gift from D. Montell (University of California, Santa Barbara, CA, USA)
UAS Sod1	#24750; BDSC
UAS Cat	#24621; BDSC
UAS lacZ	#3956; BDSC
UAS E2f1^{PIP3}	#34059; BDSC
UAS KDEL-RFP	#30909; BDSC
Pdm2-Gal4	#49828; BDSC
Xbp1>dsRed	Gift from H.D. Ryoo (NYU Grossman School of Medicine, New York, NY, USA)
UAS Xbp1-EGFP	#60731; BDSC
scrib^{1}	Gift from D. Bilder (University of California, Berkeley, CA, USA)
scrib^{j7B3}	#12159; BDSC
Act > y+>Gal4	#3953; BDSC

The detailed genotypes and incubation condition were claimed in Table S1.

Immunohistochemistry and imaging

Wing discs of third larvae were dissected in 1*PBS, then fixed in 4% formaldehyde in PBS for 20 min at room temperature. After washing with 1*PBS with 0.2% Triton X-100 (PBT), samples were incubated in PBT with primary antibodies at 4°C overnight with shaking. Then washed in PBT three times for 15 min each before

added secondary antibodies and incubated overnight at 4°C. Samples were mounted after three times wash with PBT and imaged with Zeiss LSM 800 or LSM 900 Confocal Microscope. Primary antibodies were used at the following dilutions: rabbit anti-cDcp1 (#9578S; Cell Signaling, 1:200), rat anti-Ci (DSHB, 1:20), and mouse anti-Mmp1 (mix of 3A6B4, 3B8D12, and 5H7B11) (DSHB, 1:40). The secondary antibodies conjugated with Alexa 546 or 633 (Invitrogen) were diluted 1:400. Nuclei were labeled with DAPI (Invitrogen, 1:1,000).

Live imaging

Wing discs from third instar larvae were dissected in Schneider *Drosophila* Medium (#25-512; Genesee Scientific), mounted with 1% low-melting agarose, and immersed in Schneider *Drosophila* Medium containing 5% fly extract and 1x penicillin-streptomycin antibiotics (filtered by 0.2-μm filter) as previously described (Wang et al., 2021). Live images were taken with a Zeiss LSM 980 Confocal Microscope. Projection images were used in the videos.

To quantify the dynamic behaviors observed during live imaging, we analyzed the centroid displacement speed of clones by measuring the displacement distance (defined as the movement of the clone edge along its predominant direction of extension) and dividing it by the elapsed time.

DHE staining

DHE labeling was performed as described (Diwanji and Bergmann, 2020). Wing imaginal discs were dissected in Schneider *Drosophila* Medium (#25-512; Genesee Scientific), followed by incubation in 10 μM DHE (#D11347; Thermo Fisher Scientific) and Hoechst (#33342; Thermo Fisher Scientific) in Schneider *Drosophila* Medium for 10 min in the dark. After washing with 1x PBS, samples were mounted and imaged immediately.

Fluorescence-activated cell-sorting analysis

Wing discs from third instar larvae were dissected in Schneider *Drosophila* Medium (#25-512; Genesee Scientific) and washed with EBSS. Samples were then treated with papain (50 U/ml in EBSS) and pipetted up and down intermittently at room temperature until the tissues were completely dissociated. After passing through a 40-μm filter, cells were collected by centrifugation at 1,300 rpm for 20 min and fixed with 4% formaldehyde in PBS with Hoechst 33342 (1:2,000, Invitrogen) for 30 min, followed by washing with EBSS. Cell ploidy was detected by a flow cytometer based on excitations of Hoechst (405 nm) and GFP (488 nm).

Fluorescence intensity analysis

Images were acquired using Zeiss LSM 800 and LSM 980 confocal microscopes. Mean fluorescence intensity from each section was quantified using ImageJ (Fiji) software. Relative mean fluorescence intensity = mean fluorescence intensity of target region (GFP^+) - mean fluorescence intensity of neighbor region (GFP^-).

NAC fed assay

To prevent ROS accumulation, we prepared standard food supplemented with N-acetyl cysteine (A9165; Sigma-Aldrich) at a final concentration of 100 μM.

Protein synthesis detecting

Click-iT Plus OPP Protein Synthesis Assay Kits (#C10458; Invitrogen) were used to detect and characterize newly synthesized proteins. Samples were processed according to the manufacturer's instructions.

Cell migration assay

Cell invasion assays were performed using Boyden chambers as previously described (Tan et al., 2023). Briefly, 2,000 cells were seeded in 200 μl of serum-free medium in chambers and allowed to migrate toward completed medium in the bottom wells for 16 h. Migrated cells on the bottom side of the membrane were fixed in 90% ethanol, stained with 0.1% crystal violet, imaged, and quantified.

Western blot

Cells were lysed in 1× RIPA buffer (Cell Signaling) supplemented with protease and phosphatase inhibitors. Equal amounts of protein were separated by SDS-PAGE and transferred onto a nitrocellulose membrane. The membrane was blocked with 5% milk for 30 min at room temperature, followed by overnight incubation at 4°C with primary antibodies against pJNK (#9251; Cell Signaling), JNK (#9252; Cell Signaling), or Tubulin (11224-1-AP; Proteintech). After washing, membranes were incubated with HRP-conjugated secondary antibodies for 1 h at room temperature. Protein bands were detected using an enhanced chemiluminescence (ECL) detection system (Thermo Fisher Scientific) and imaged with a ChemiDoc Imaging System (Bio-Rad).

Gamma (γ)-ray irradiation

Adult flies were exposed to a single dose of γ-ray (18 Gy) using a Gammacell 40 Cs-137 irradiator (MDS Nordion) with a dose rate of 36 Gy/h. Flies were dissected 24 h after irradiation.

Quantification and statistical analysis

All data were analyzed with the GraphPad Prism (GraphPad Software). Unpaired Student *t*-test (two-tailed) was used for comparisons between two samples, and one-way ANOVA with Dunnett's multiple comparisons test was used for multiple group comparisons.

All images were processed with ImageJ (Fiji).

Online supplemental material

Fig. S1 shows induced polyploidy by *fzr* or *rux* overexpression results in basal cellular protrusions. Fig. S2 shows JNK activation in induced polyploid cells. Fig. S3 shows ROS-mediated JNK activation in induced polyploid cells. Fig. S4 shows that elevated ER stress drives ROS production in induced polyploid cells. Fig. S5 shows that induced polyploid cells exhibit active engulfment. Table S1 shows detailed genotypes for each experiment. Video 3 shows time-lapse video of *lacZ-OE* control cells. Video 1 shows time-lapse video of *fzr-OE* polyploid cell dynamics. Video 2 shows time-lapse video of *rux-OE* polyploid cell dynamics. Video 4 shows induced polyploid cells navigating around the trachea. Video 5 shows time-lapse video showing JNK activation in a *fzr-OE* polyploid cell. Video 6 shows time-lapse video

showing JNK activation in *rux-OE* polyploid cells. Video 7 shows time-lapse video showing *mahj*[1] cells engulfed by *fzr-OE* polyploid cells.

Data availability

All data needed to evaluate the conclusions in the paper are included in the main text and/or the supplemental materials.

Acknowledgments

We thank D. Bilder, D. Bohmann, D. Fox, D. Montell, H.D. Ryoo, the Bloomington *Drosophila* Stock Center, and the Developmental Studies Hybridoma Bank for providing fly lines and antibodies. We also acknowledge FlyBase for essential genetic and genomic information. Special thanks to Dr. B. Calvi for helpful discussions regarding the results and their implications.

This work was supported in part by the National Institutes of Health (grants CA227789, CA224381, CA287524, and GM072562 to W.-M. Deng and R03CA280382 to X. Tan), the Ladies Leukemia League, an LCRC seed grant to W.-M. Deng, and a Tulane COR Research Fellowships to X. Tan, and Japan Society for the Promotion of Science (JSPS) KAKENHI (grants JP22KK0110, JP23K24080, JP23K18238) to Y. Tamori.

Author contributions: Youfang Zhou: conceptualization, data curation, formal analysis, investigation, methodology, project administration, supervision, validation, visualization, and writing—original draft, review, and editing. Xianfeng Wang: conceptualization, data curation, formal analysis, investigation, methodology, validation, visualization, and writing—original draft, review, and editing. Xiaochao Tan: data curation, formal analysis, funding acquisition, investigation, methodology, and writing—original draft. Shingo Nara: conceptualization, data curation, formal analysis, investigation, methodology, and resources. Yi-Chun Huang: resources and writing—review and editing. Yoichiro Tamori: data curation, formal analysis, funding acquisition, investigation, methodology, resources, validation, visualization, and writing—review and editing. Wu-Min Deng: conceptualization, funding acquisition, methodology, project administration, supervision, and writing—original draft, review, and editing.

Disclosures: The authors declare no competing interests exist.

Submitted: 15 July 2025
Revised: 18 January 2026
Accepted: 27 February 2026

References

Aldini, G., A. Altomare, G. Baron, G. Vistoli, M. Carini, L. Borsani, and F. Sergio. 2018. N-Acetylcysteine as an antioxidant and disulphide breaking agent: The reasons why. *Free Radic. Res.* 52:751–762. https://doi.org/10.1080/10715762.2018.1468564

Alexandre, C., A. Baena-Lopez, and J.-P. Vincent. 2014. Patterning and growth control by membrane-tethered wingless. *Nature*. 505:180–185. https://doi.org/10.1038/nature12879

Alkafaas, S.S., S.A. Khedr, S.S. ElKafas, W. Hafez, S.A. Loutfy, M. Sakran, and N. Janković. 2024. Targeting JNK kinase inhibitors via molecular docking: A promising strategy to address tumorigenesis and drug resistance. *Bioorg. Chem.* 153:107776. https://doi.org/10.1016/j.bioorg.2024.107776

Anatskaya, O.V., and A.E. Vinogradov. 2022. Polyploidy as a fundamental phenomenon in evolution, development, adaptation and diseases. *Int. J. Mol. Sci.* 23:3542. https://doi.org/10.3390/ijms23073542

Andersen, D.S., J. Colombani, V. Palmerini, K. Chakrabandhu, E. Boone, M. Röthlisberger, J. Toggweiler, K. Basler, M. Mapelli, A.O. Hueber, and P. Léopold. 2015. The *Drosophila* TNF receptor Grindelwald couples loss of cell polarity and neoplastic growth. *Nature*. 522:482–486. https://doi.org/10.1038/nature14298

Bergmann, A., H.D. Ryoo, J. Li, and M.-J. Kang. 2013. *Drosophila* XBP1 expression reporter marks cells under endoplasmic reticulum stress and with high protein secretory load. *PLoS One*. 8:e75774. https://doi.org/10.1371/journal.pone.0075774

Bukkuri, A., K.J. Pienta, R.H. Austin, E.U. Hammarlund, S.R. Amend, and J.S. Brown. 2023. A mathematical investigation of polyaneuploid cancer cell memory and cross-resistance in state-structured cancer populations. *Sci. Rep.* 13:15027. https://doi.org/10.1038/s41598-023-42368-8

Buszczak, M., and L. Cooley. 2000. Eggs to die for: cell death during *Drosophila* oogenesis. *Cell Death Differ.* 7:1071–1074. https://doi.org/10.1038/sj.cdd.4400755

Cao, J., J. Wang, C.P. Jackman, A.H. Cox, M.A. Trembley, J.J. Balowski, B.D. Cox, A. De Simone, A.L. Dickson, S. Di Talia, et al. 2017. Tension creates an endoreplication wavefront that leads regeneration of epicardial tissue. *Dev. Cell*. 42:600–615.e4. https://doi.org/10.1016/j.devcel.2017.08.024

Chatterjee, N., and D. Bohmann. 2012. A versatile ΦC31 based reporter system for measuring AP-1 and Nrf2 signaling in *Drosophila* and in tissue culture. *PLoS One*. 7:e34063. https://doi.org/10.1371/journal.pone.0034063

Chen, X., C. Shi, M. He, S. Xiong, and X. Xia. 2023. Endoplasmic reticulum stress: Molecular mechanism and therapeutic targets. *Signal. Transduct. Target. Ther.* 8:352. https://doi.org/10.1038/s41392-023-01570-w

Darmasaputra, G.S., L.M. van Rijnberk, and M. Galli. 2024. Functional consequences of somatic polyploidy in development. *Development*. 151:dev202392. https://doi.org/10.1242/dev.202392

de Vreede, G., H.A. Morrison, A.M. Houser, R.M. Boileau, D. Andersen, J. Colombani, and D. Bilder. 2018. A *Drosophila* tumor suppressor gene prevents tonic TNF signaling through receptor N-Glycosylation. *Dev. Cell*. 45:595–605.e4. https://doi.org/10.1016/j.devcel.2018.05.012

Deng, H., S. Takashima, M. Paul, M. Guo, and V. Hartenstein. 2018. Mitochondrial dynamics regulates *Drosophila* intestinal stem cell differentiation. *Cell Death Discov.* 4:17. https://doi.org/10.1038/s41420-018-0083-0

Diwanji, N., and A. Bergmann. 2020. Basement membrane damage by ROS- and JNK-mediated Mmp2 activation drives macrophage recruitment to overgrown tissue. *Nat. Commun.* 11:3631. https://doi.org/10.1038/s41467-020-17399-8

Donne, R., M. Saroul-Aïnama, P. Cordier, S. Celton-Morizur, and C. Desdouets. 2020. Polyploidy in liver development, homeostasis and disease. *Nat. Rev. Gastroenterol. Hepatol.* 17:391–405. https://doi.org/10.1038/s41575-020-0284-x

Duncan, A.W., M.H. Taylor, R.D. Hickey, A.E. Hanlon Newell, M.L. Lenzi, S.B. Olson, M.J. Finegold, and M. Grompe. 2010. The ploidy conveyor of mature hepatocytes as a source of genetic variation. *Nature*. 467:707–710. https://doi.org/10.1038/nature09414

Eichenlaub, T., S.M. Cohen, and H. Herranz. 2016. Cell competition drives the formation of metastatic tumors in a *Drosophila* model of epithelial tumor formation. *Curr. Biol.* 26:419–427. https://doi.org/10.1016/j.cub.2015.12.042

Elia, A., S. Mohsin, and M. Khan. 2023. Cardiomyocyte ploidy, metabolic reprogramming and heart repair. *Cells*. 12:1571. https://doi.org/10.3390/cells12121571

Fogarty, C.E., N. Diwanji, J.L. Lindblad, M. Tare, A. Amcheslavsky, K. Makhijani, K. Brückner, Y. Fan, and A. Bergmann. 2016. Extracellular reactive oxygen species drive apoptosis-induced proliferation via *Drosophila* macrophages. *Curr. Biol.* 26:575–584. https://doi.org/10.1016/j.cub.2015.12.064

Garcia-Arias, J.M., N. Pinal, S. Cristobal-Vargas, C. Estella, and G. Morata. 2023. Lack of apoptosis leads to cellular senescence and tumorigenesis in *Drosophila* epithelial cells. *Cell Death Discov.* 9:281. https://doi.org/10.1038/s41420-023-01583-y

Germani, F., C. Bergantinos, and L.A. Johnston. 2018. Mosaic analysis in *Drosophila*. *Genetics*. 208:473–490. https://doi.org/10.1534/genetics.117.300256

Giannakakou, P., R. Robey, T. Fojo, and M.V. Blagosklonny. 2001. Low concentrations of paclitaxel induce cell type-dependent p53, p21 and G1/G2 arrest instead of mitotic arrest: Molecular determinants of paclitaxel-

induced cytotoxicity. *Oncogene*. 20:3806–3813. https://doi.org/10.1038/sj.onc.1204487
Gjelsvik, K.J., R. Besen-McNally, and V.P. Losick. 2019. Solving the polyploid mystery in health and disease. *Trends Genet.* 35:6–14. https://doi.org/10.1016/j.tig.2018.10.005
Herrera, S.C., and E.A. Bach. 2021. The emerging roles of JNK signaling in *Drosophila* stem cell homeostasis. *Int. J. Mol. Sci.* 22:5519. https://doi.org/10.3390/ijms22115519
Herriage, H.C., Y.-T. Huang, and B.R. Calvi. 2024. The antagonistic relationship between apoptosis and polyploidy in development and cancer. *Semin. Cell Dev. Biol.* 156:35–43. https://doi.org/10.1016/j.semcdb.2023.05.009
Huang, Y.-C., C. Almeida Machado Costa, N. Vergara Ruiz, X. Wang, A. Jevitt, C.M. Breneman, C. Han, and W.M. Deng. 2025. Polyploidy promotes transformation of epithelial cells into nonprofessional phagocytes. *Proc. Natl. Acad. Sci. USA*. 122:e2427293122. https://doi.org/10.1073/pnas.2427293122
Huang, Y.-T., L.L. Hesting, and B.R. Calvi. 2024. An unscheduled switch to endocycles induces a reversible senescent arrest that impairs growth of the *Drosophila* wing disc. *PLoS Genet.* 20:e1011387. https://doi.org/10.1371/journal.pgen.1011387
Jemaà, M., R. Daams, S. Charfi, F. Mertens, S.M. Huber, and R. Massoumi. 2023. Tetraploidization increases the motility and invasiveness of cancer cells. *Int. J. Mol. Sci.* 24:13926. https://doi.org/10.3390/ijms241813926
Johansen, K.M., W. Cai, H. Deng, X. Bao, W. Zhang, J. Girton, and J. Johansen. 2009. Polytene chromosome squash methods for studying transcription and epigenetic chromatin modification in *Drosophila* using antibodies. *Methods*. 48:387–397. https://doi.org/10.1016/j.ymeth.2009.02.019
Kroemer, G., and J.-L. Perfettini. 2014. Entosis, a key player in cancer cell competition. *Cell Res.* 24:1280–1281. https://doi.org/10.1038/cr.2014.133
Kurucz, E., R. Márkus, J. Zsámboki, K. Folkl-Medzihradszky, Z. Darula, P. Vilmos, A. Udvardy, I. Krausz, T. Lukacsovich, E. Gateff, et al. 2007. Nimrod, a putative phagocytosis receptor with EGF repeats in *Drosophila* plasmatocytes. *Curr. Biol.* 17:649–654. https://doi.org/10.1016/j.cub.2007.02.041
La Marca, J.E., and H.E. Richardson. 2020. Two-Faced: Roles of JNK signalling during tumourigenesis in the *Drosophila* model. *Front. Cell Dev. Biol.* 8:42. https://doi.org/10.3389/fcell.2020.00042
Li, W., and N.E. Baker. 2007. Engulfment is required for cell competition. *Cell*. 129:1215–1225. https://doi.org/10.1016/j.cell.2007.03.054
Liu, P., L. Wang, and H. Yu. 2024. Polyploid giant cancer cells: Origin, possible pathways of formation, characteristics, and mechanisms of regulation. *Front. Cell Dev. Biol.* 12:1410637. https://doi.org/10.3389/fcell.2024.1410637
Llense, F., and E. Martín-Blanco. 2008. JNK signaling controls border cell cluster integrity and collective cell migration. *Curr. Biol.* 18:538–544. https://doi.org/10.1016/j.cub.2008.03.029
Loker, R., and R.S. Mann. 2022. Divergent expression of paralogous genes by modification of shared enhancer activity through a promoter-proximal silencer. *Curr. Biol.* 32:3545–3555.e4. https://doi.org/10.1016/j.cub.2022.06.069
Losick, V.P. 2016. Wound-induced polyploidy is required for tissue repair. *Adv. Wound Care*. 5:271–278. https://doi.org/10.1089/wound.2014.0545
Losick, V.P., D.T. Fox, and A.C. Spradling. 2013. Polyploidization and cell fusion contribute to wound healing in the adult *Drosophila* epithelium. *Curr. Biol.* 23:2224–2232. https://doi.org/10.1016/j.cub.2013.09.029
Melcarne, C., B. Lemaitre, and E. Kurant. 2019. Phagocytosis in *Drosophila*: From molecules and cellular machinery to physiology. *Insect Biochem. Mol. Biol.* 109:1–12. https://doi.org/10.1016/j.ibmb.2019.04.002
Miao, G., L. Guo, and D.J. Montell. 2022. Border cell polarity and collective migration require the spliceosome component Cactin. *J. Cell Biol.* 221:e202202146. https://doi.org/10.1083/jcb.202202146
Milano, S.N., L.V. Bayer, J.J. Ko, C.E. Casella, and D.P. Bratu. 2025. The role of ER exit sites in maintaining P-body organization and integrity during *Drosophila* melanogaster oogenesis. *EMBO Rep.* 26:494–520. https://doi.org/10.1038/s44319-024-00344-x
Moein, S., R. Adibi, L. da Silva Meirelles, N.B. Nardi, and Y. Gheisari. 2020. Cancer regeneration: Polyploid cells are the key drivers of tumor progression. *Biochim. Biophys. Acta Rev. Cancer*. 1874:188408. https://doi.org/10.1016/j.bbcan.2020.188408
Montell, D.J. 2003. Border-cell migration: The race is on. *Nat. Rev. Mol. Cell Biol.* 4:13–24. https://doi.org/10.1038/nrm1006
Nagata, R., and T. Igaki. 2018. Cell competition: Emerging mechanisms to eliminate neighbors. *Dev. Growth Differ.* 60:522–530. https://doi.org/10.1111/dgd.12575
Nandakumar, S., O. Grushko, and L.A. Buttitta. 2020. Polyploidy in the adult *Drosophila* brain. *eLife*. 9:e54385. https://doi.org/10.7554/eLife.54385
Okamoto, N., N. Yamanaka, Y. Yagi, Y. Nishida, H. Kataoka, M.B. O'Connor, and A. Mizoguchi. 2009. A fat body-derived IGF-like peptide regulates postfeeding growth in *Drosophila*. *Dev. Cell*. 17:885–891. https://doi.org/10.1016/j.devcel.2009.10.008
Overholtzer, M., A.A. Mailleux, G. Mouneimne, G. Normand, S.J. Schnitt, R.W. King, E.S. Cibas, and J.S. Brugge. 2007. A nonapoptotic cell death process, entosis, that occurs by cell-in-cell invasion. *Cell*. 131:966–979. https://doi.org/10.1016/j.cell.2007.10.040
Paro, R. 2008. Mapping protein distributions on polytene chromosomes by immunostaining. *CSH Protoc.* 2008:prot4714. https://doi.org/10.1101/pdb.prot4714
Peterson, N.G., and D.T. Fox. 2021. Communal living: The role of polyploidy and syncytia in tissue biology. *Chromosome Res.* 29:245–260. https://doi.org/10.1007/s10577-021-09664-3
Pienta, K.J., E.U. Hammarlund, R.H. Austin, R. Axelrod, J.S. Brown, and S.R. Amend. 2022. Cancer cells employ an evolutionarily conserved polyploidization program to resist therapy. *Semin. Cancer Biol.* 81:145–159. https://doi.org/10.1016/j.semcancer.2020.11.016
Pinal, N., M. Martín, I. Medina, and G. Morata. 2018. Short-term activation of the Jun N-terminal kinase pathway in apoptosis-deficient cells of *Drosophila* induces tumorigenesis. *Nat. Commun.* 9:1541. https://doi.org/10.1038/s41467-018-04000-6
Roh, M., R. van der Meer, and S.A. Abdulkadir. 2012. Tumorigenic polyploid cells contain elevated ROS and ARE selectively targeted by antioxidant treatment. *J. Cell Physiol.* 227:801–812. https://doi.org/10.1002/jcp.22793
Santabárbara-Ruiz, P., M. López-Santillán, I. Martínez-Rodríguez, A. Binagui-Casas, L. Pérez, M. Milán, M. Corominas, and F. Serras. 2015. ROS-Induced JNK and p38 signaling is required for unpaired cytokine activation during *Drosophila* regeneration. *PLoS Genet.* 11:e1005595. https://doi.org/10.1371/journal.pgen.1005595
Santoni, M.-J., R. Kashyap, L. Camoin, and J.-P. Borg. 2020. The scribble family in cancer: Twentieth anniversary. *Oncogene*. 39:7019–7033. https://doi.org/10.1038/s41388-020-01478-7
Schaeffer, V., C. Althauser, H.R. Shcherbata, W.-M. Deng, and H. Ruohola-Baker. 2004. Notch-dependent Fizzy-Related/Hec1/Cdh1 expression is required for the mitotic-to-endocycle transition in *Drosophila* follicle cells. *Curr. Biol.* 14:630–636. https://doi.org/10.1016/j.cub.2004.03.040
Shcherbata, H.R., C. Althauser, S.D. Findley, and H. Ruohola-Baker. 2004. The mitotic-to-endocycle switch in *Drosophila* follicle cells is executed by notch-dependent regulation of G1/S, G2/M and M/G1 cell-cycle transitions. *Development*. 131:3169–3181. https://doi.org/10.1242/dev.01172
Shibutani, S.T., A.F. de la Cruz, V. Tran, W.J. Turbyfill 3rd, T. Reis, B.A. Edgar, and R.J. Duronio. 2008. Intrinsic negative cell cycle regulation provided by PIP box- and Cul4Cdt2-mediated destruction of E2f1 during S phase. *Dev. Cell*. 15:890–900. https://doi.org/10.1016/j.devcel.2008.10.003
Shields, H.J., A. Traa, and J.M. Van Raamsdonk. 2021. Beneficial and detrimental effects of reactive oxygen species on lifespan: A comprehensive review of comparative and experimental studies. *Front. Cell Dev. Biol.* 9:628157. https://doi.org/10.3389/fcell.2021.628157
Shinomiya, N. 2007. New concepts in radiation-induced apoptosis: 'pre-mitotic apoptosis' and 'postmitotic apoptosis. *J. Cell. Mol. Med.* 5:240–253. https://doi.org/10.1111/j.1582-4934.2001.tb00158.x
Slaidina, M., R. Delanoue, S. Gronke, L. Partridge, and P. Léopold. 2009. A *Drosophila* insulin-like peptide promotes growth during nonfeeding states. *Dev. Cell*. 17:874–884. https://doi.org/10.1016/j.devcel.2009.10.009
Sykiotis, G.P., and D. Bohmann. 2008. Keap1/Nrf2 signaling regulates oxidative stress tolerance and lifespan in *Drosophila*. *Dev. Cell*. 14:76–85. https://doi.org/10.1016/j.devcel.2007.12.002
Tamori, Y., C.U. Bialucha, A.G. Tian, M. Kajita, Y.C. Huang, M. Norman, N. Harrison, J. Poulton, K. Ivanovitch, L. Disch, et al. 2010. Involvement of Lgl and Mahjong/VprBP in cell competition. *PLoS Biol.* 8:e1000422. https://doi.org/10.1371/journal.pbio.1000422
Tamori, Y., and W.M. Deng. 2013. Tissue repair through cell competition and compensatory cellular hypertrophy in postmitotic epithelia. *Dev. Cell*. 25:350–363. https://doi.org/10.1016/j.devcel.2013.04.013
Tamori, Y., and W.-M. Deng. 2014. Compensatory cellular hypertrophy: The other strategy for tissue homeostasis. *Trends Cell Biol.* 24:230–237. https://doi.org/10.1016/j.tcb.2013.10.005
Tamori, Y., E. Suzuki, and W.M. Deng. 2016. Epithelial tumors originate in tumor hotspots, a tissue-intrinsic microenvironment. *PLoS Biol.* 14:e1002537. https://doi.org/10.1371/journal.pbio.1002537

Tan, X., G.Y. Xiao, S. Wang, L. Shi, Y. Zhao, X. Liu, J. Yu, W.K. Russell, C.J. Creighton, and J.M. Kurie. 2023. EMT-activated secretory and endocytic vesicular trafficking programs underlie a vulnerability to PI4K2A antagonism in lung cancer. *J. Clin. Invest.* 133:e165863. https://doi.org/10.1172/JCI165863

Thannickal, V.J., and B.L. Fanburg. 2000. Reactive oxygen species in cell signaling. *Am. J. Physiol. Lung. Cell. Mol. Physiol.* 279:L1005–L1028. https://doi.org/10.1152/ajplung.2000.279.6.L1005

Tripathi, B.K., K.D. Irvine, and C. Thummel. 2022. The wing imaginal disc. *Genetics*. 220:iyac020. https://doi.org/10.1093/genetics/iyac020

van Neerven, S.M., and L. Vermeulen. 2023. Cell competition in development, homeostasis and cancer. *Nat. Rev. Mol. Cell Biol.* 24:221–236. https://doi.org/10.1038/s41580-022-00538-y

Verheij, M., and H. Bartelink. 2000. Radiation-induced apoptosis. *Cell Tissue Res.* 301:133–142. https://doi.org/10.1007/s004410000188

Wang, X., H. Bao, Y.-C. Huang, A. Barua, C.-M. Lai, J. Sun, Y. Zhou, F. Cong, S. Gong, C.-H. Chang, and W.-M. Deng. 2024. Sex-dimorphic tumor growth is regulated by tumor microenvironmental and systemic signals. *Sci. Adv.* 10:eads4229. https://doi.org/10.1126/sciadv.ads4229

Wang, X.-F., S.-A. Yang, S. Gong, C.-H. Chang, J.M. Portilla, D. Chatterjee, J. Irianto, H. Bao, Y.-C. Huang, and W.-M. Deng. 2021. Polyploid mitosis and depolyploidization promote chromosomal instability and tumor progression in a Notch-induced tumor model. *Dev. Cell*. 56:1976–1988.e4. https://doi.org/10.1016/j.devcel.2021.05.017

Wang, Y., and Y. Tamori. 2024. Polyploid cancer cell models in *Drosophila*. *Genes*. 15:96. https://doi.org/10.3390/genes15010096

Weber, U., N. Paricio, and M. Mlodzik. 2000. Jun Mediates Frizzled-induced R3/R4 cell fate distinction and planar polarity determination in the *Drosophila* eye. *Development*. 127:3619–3629. https://doi.org/10.1242/dev.127.16.3619

Zhang, B., S. Mehrotra, W.L. Ng, and B.R. Calvi. 2014a. Low levels of p53 protein and chromatin silencing of p53 target genes repress apoptosis in *Drosophila* endocycling cells. *PLoS Genet.* 10:e1004581. https://doi.org/10.1371/journal.pgen.1004581

Zhang, S., I. Mercado-Uribe, Z. Xing, B. Sun, J. Kuang, and J. Liu. 2014b. Generation of cancer stem-like cells through the formation of polyploid giant cancer cells. *Oncogene*. 33:116–128. https://doi.org/10.1038/onc.2013.96

Zielke, N., K.J. Kim, V. Tran, S.T. Shibutani, M.J. Bravo, S. Nagarajan, M. van Straaten, B. Woods, G. von Dassow, C. Rottig, et al. 2011. Control of *Drosophila* endocycles by E2F and CRL4(CDT2). *Nature*. 480:123–127. https://doi.org/10.1038/nature10579

Supplemental material

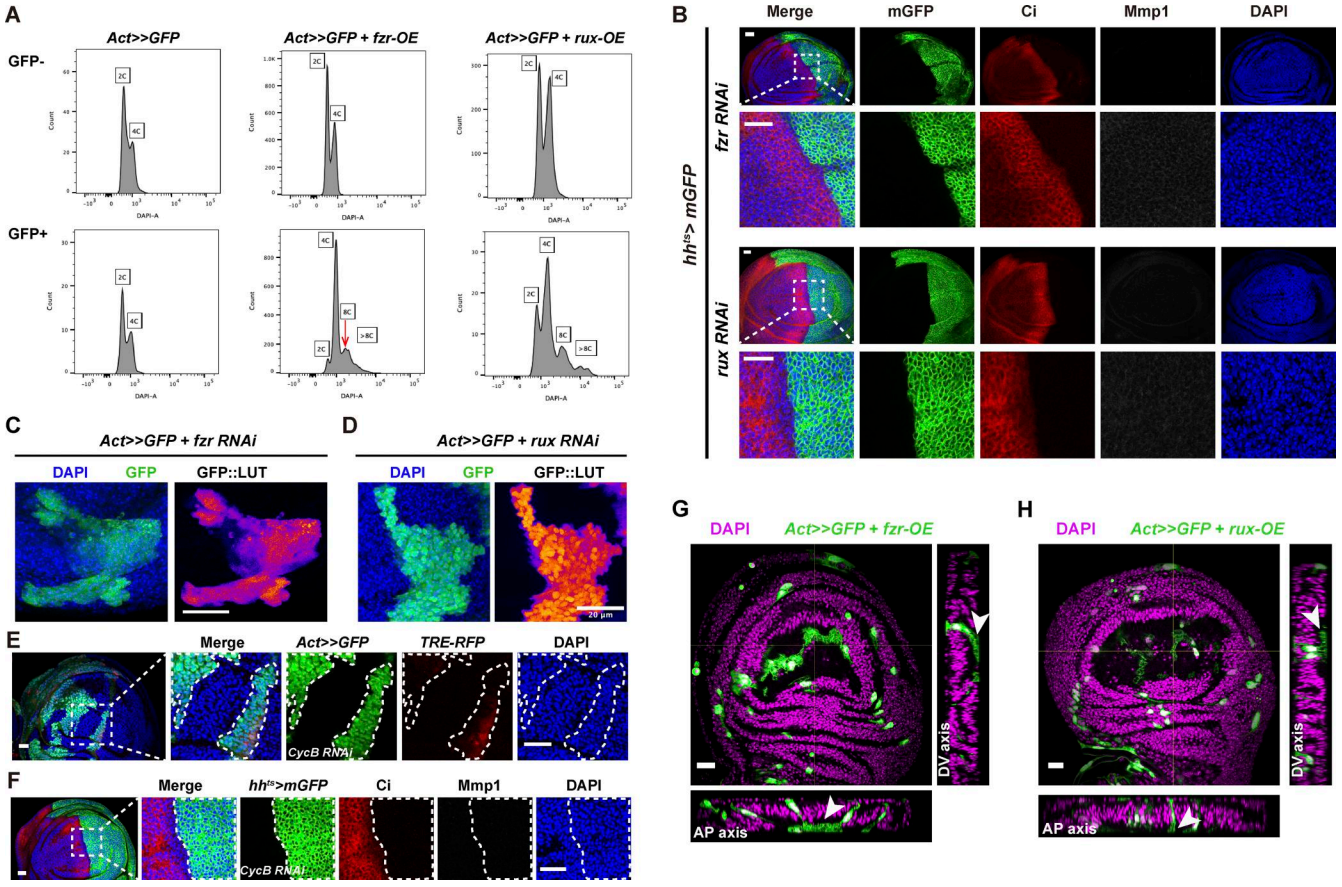

Figure S1. **Induced polyploidy by *fzr* or *rux* overexpression results in basal cellular protrusions. (A)** DAPI-based ploidy analysis of control (first column), *fzr-OE* (second column), and *rux-OE* (third column) wing discs. The first row shows ploidy in GFP$^-$ cells, while the second row shows ploidy in GFP$^+$ cells. **(B)** Confocal images of *fzr RNAi* and *rux RNAi* samples stained with Mmp1 (gray), Ci (red), and DAPI (blue). The second and fourth rows present zoomed-in views of the white dashed rectangles in the first and third rows. **(C)** Clones expressing *fzr RNAi* (green in merged image and LUT in single image) stained with DAPI (blue). **(D)** Clones expressing *rux RNAi* (green in merged image and LUT in single image) stained with DAPI (blue). **(E)** Confocal images of *Act>>GFP + TRE-RFP + CycB RNAi* disc stained with DAPI (blue). The second to fifth columns (white dashed area) present zoomed-in view of the corresponding white dashed rectangle in the first column. **(F)** Confocal images of *hh^{ts}>mGFP + CycB RNAi* disc stained with DAPI (blue) and Mmp1 (gray). The second to sixth columns (white dashed line marked anterior-posterior boundary) show zoomed-in view of the white dashed rectangle in the first column. **(G)** Confocal images of *fzr-OE* (green) stained with DAPI (magenta) with dorsal-ventral (DV) axis view and AP axis view. **(H)** Confocal images of *rux-OE* (green) stained with DAPI (magenta), shown in both DV and AP axis views. White arrowheads indicate protrusions reaching the basal side. Scale bars: 20 µm.

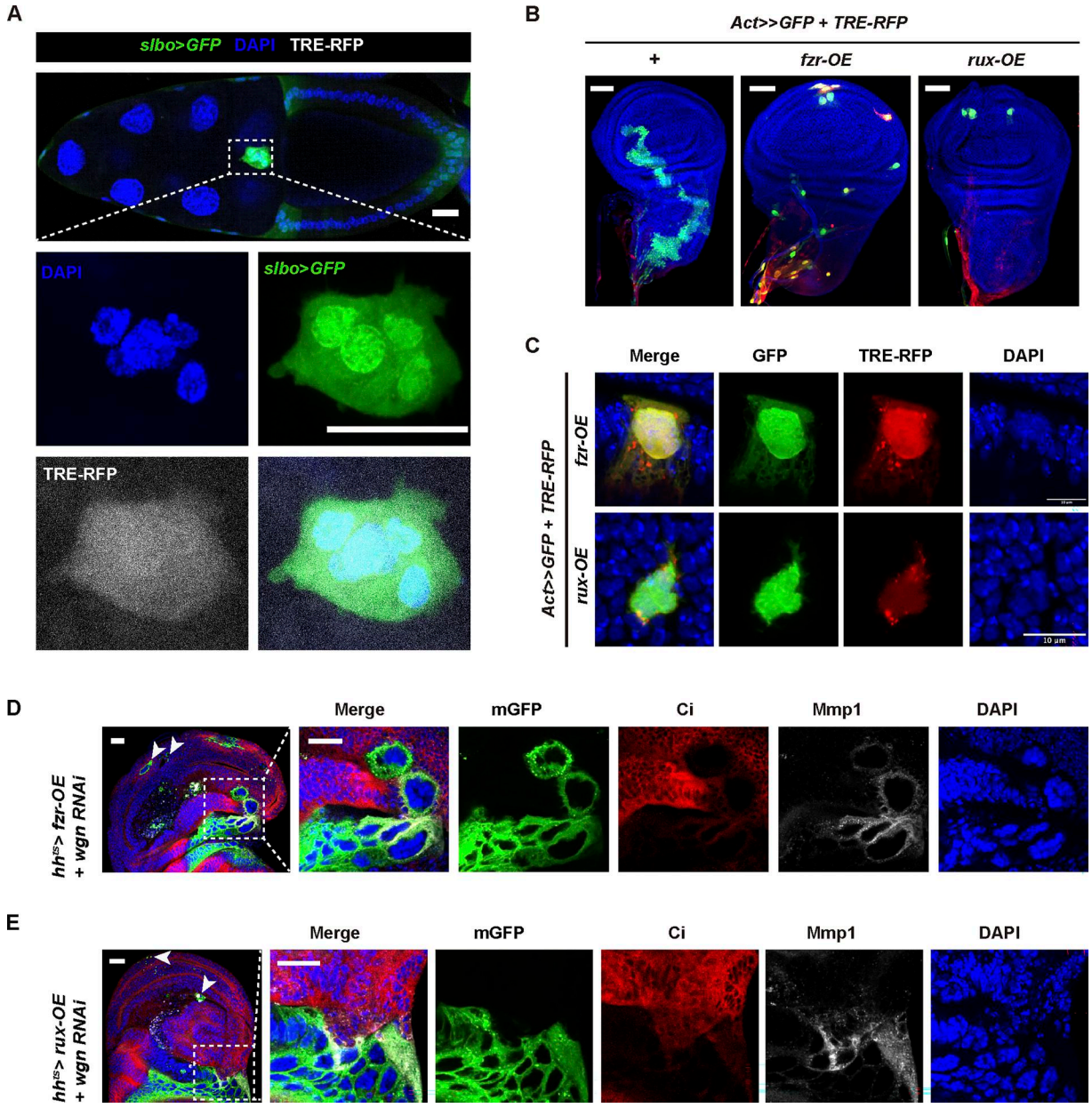

Figure S2. **JNK activation in induced polyploid cells. (A)** Egg chamber stained with DAPI (blue). Border cells are marked by GFP (green), and TRE expression is labeled by RFP (gray). The first row shows the whole egg chamber, the second and third rows are zoomed-in views of the white dashed rectangles. Scale bars: 20 µm. **(B)** Confocal images of TRE-RFP (red) in control (+), *fzr-OE* and *rux-OE* polyploidy clones (green) in whole discs. Scale bars: 50 µm. **(C)** Individual clones of *fzr-OE* and *rux-OE* showing TRE-RFP signal. Scale bars: 10 µm. **(D and E)** Confocal images of *wgn RNAi* co-expressed with *fzr-OE* (D) or *rux-OE* (E), stained with Ci (red), Mmp1 (gray), and DAPI (blue). The second to sixth columns show zoomed-in views of the white dashed rectangles in the first column. White arrowheads indicate cells crossing the AP boundary. Scale bars: 20 µm.

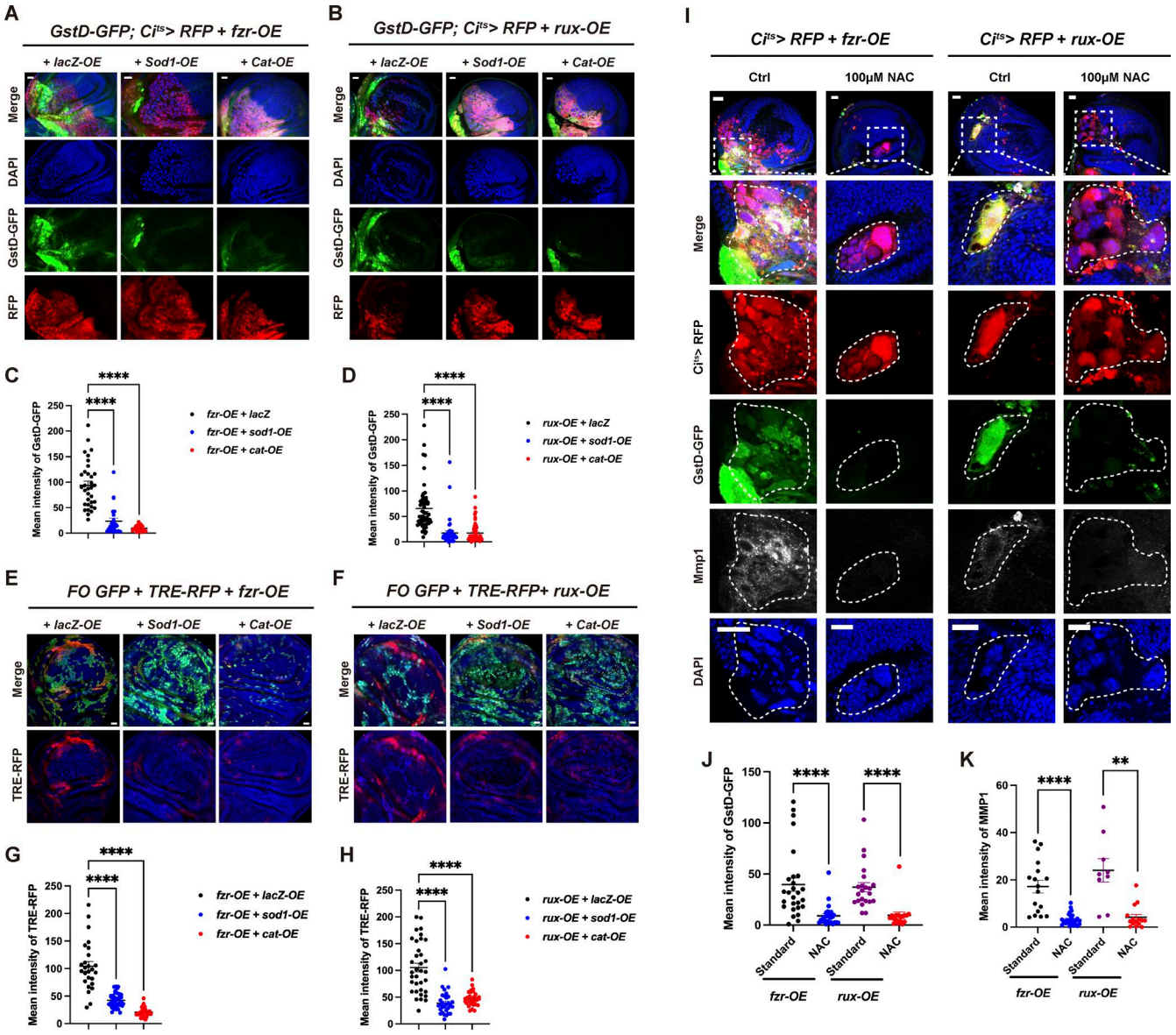

Figure S3. **ROS-mediated JNK activation in induced polyploid cells. (A)** Confocal images showing GstD-GFP expression in *fzr-OE + lacZ-OE*, *fzr-OE + sod1-OE*, or *fzr-OE + cat-OE* clones under *Ci^ts>RFP*, stained with Mmp1 (gray) and DAPI (blue). Scale bars: 20 μm. **(B)** Confocal images showing GstD-GFP expression in *rux-OE + lacZ-OE*, *rux-OE + sod1-OE*, or *rux-OE + cat-OE* under *Ci^ts>RFP*, stained with Mmp1 (gray) and DAPI (blue). Scale bars: 20 μm. **(C)** Quantification of mean intensity of GstD-GFP in *fzr-OE + lacZ-OE* (n = 33), *fzr-OE + sod1-OE* (n = 24), and *fzr-OE + cat-OE* (n = 22) clones. **(D)** Quantification of mean intensity of GstD-GFP in *rux-OE + lacZ-OE* (n = 54), *rux-OE + sod1-OE* (n = 44), and *rux-OE + cat-OE* (n = 54) clones. **(E)** Confocal images showing TRE-RFP level in *fzr-OE + lacZ-OE*, *fzr-OE + Sod1-OE*, or *fzr-OE + Cat-OE* wing discs. Scale bars: 20 μm. **(F)** Confocal images showing TRE-RFP levels in *rux-OE + lacZ-OE*, *rux-OE + sod1-OE*, or *rux-OE + cat-OE* wing discs. Scale bars: 20 μm. **(G)** Quantification of mean intensity of TRE-RFP in *fzr-OE + lacZ-OE* (n = 26), *fzr-OE + Sod1-OE* (n = 37), or *fzr-OE + Cat-OE* (n = 28) wing discs. **(H)** Quantification of mean intensity of TRE-RFP in *rux-OE + lacZ-OE* (n = 35), *rux-OE + Sod1-OE* (n = 30), or *rux-OE + Cat-OE* (n = 31) wing discs. Data in C, D, G, and H are presented as mean ± SEM, analyzed by one-way ANOVA. **** represents P value <0.0001. **(I)** Confocal images showing GstD-GFP expression in *fzr-OE* or *rux-OE* clones fed with either normal food or NAC-containing food. Samples were stained with Mmp1 (gray) and DAPI (blue). White dashed outlines indicate polyploid clones. The second to sixth rows show zoomed-in views of the white dashed rectangles. Scale bars: 20 μm. **(J)** Quantification of mean intensity of GstD-GFP in *fzr-OE* or *rux-OE* clones under standard conditions (n = 27 for *fzr-OE* and n = 22 for *rux-OE*) or following NAC feeding (n = 26 for *fzr-OE* and n = 17 for *rux-OE*). **(K)** Quantification of mean intensity of Mmp1 in *fzr-OE* or *rux-OE* clones under standard conditions (n = 17 for *fzr-OE* and n = 9 for *rux-OE*) or following NAC feeding (n = 27 for *fzr-OE* and n = 15 for *rux-OE*). Data in J and K are presented as mean ± SEM and analyzed using an unpaired two-tailed *t* test in two groups. ** represents P value = 0.0037; **** represents P value <0.0001.

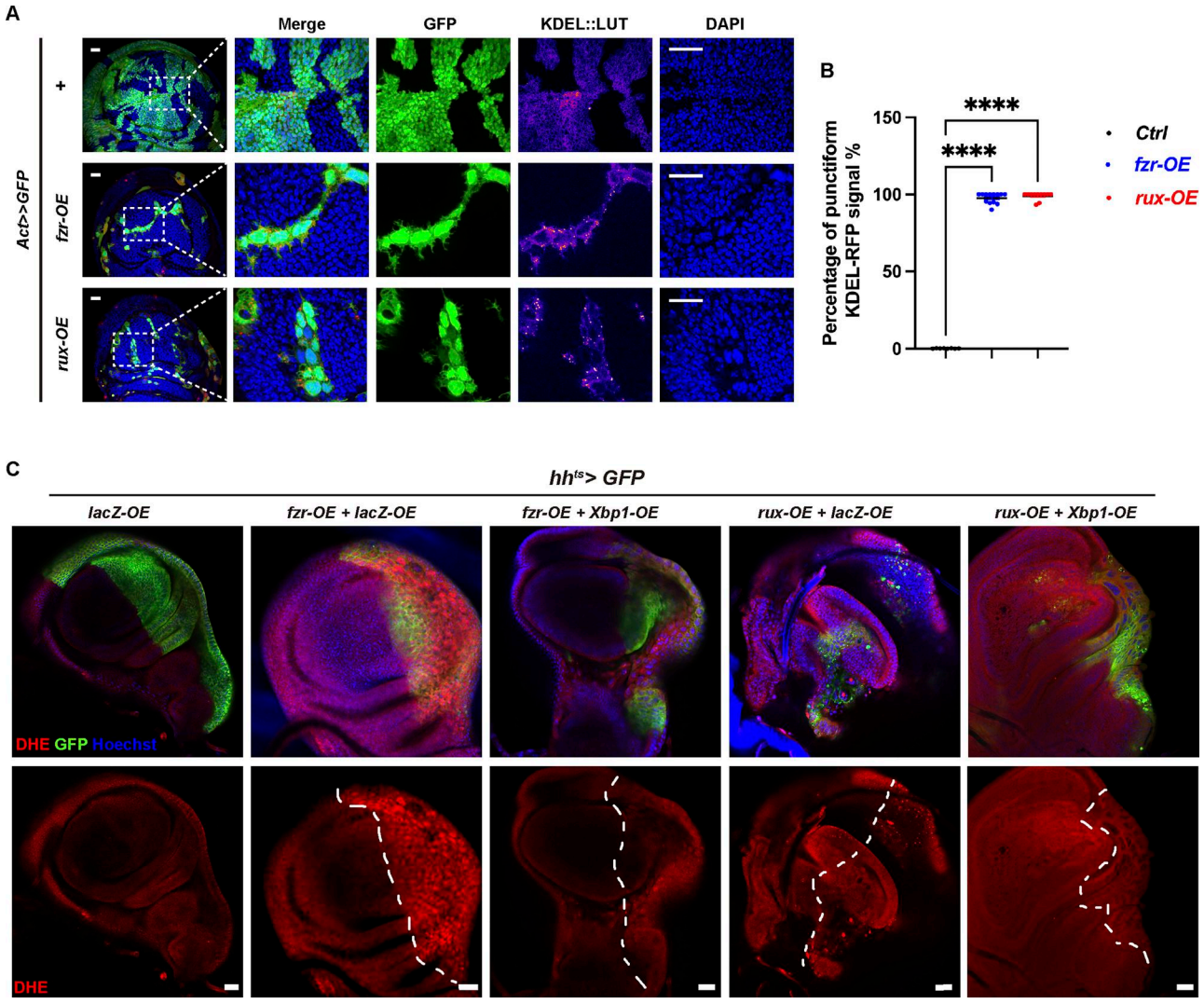

Figure S4. **Elevated ER stress drives ROS production in induced polyploid cells. (A)** Confocal images showing KDEL-RFP (red in merged images and LUT in separated channels) expression in *fzr-OE* or *rux-OE* GFP clones (green) compared with control (+). Samples were stained with DAPI (blue). The second to fifth columns show zoomed-in views of the white dashed rectangles in the first column. Scale bars: 20 µm. **(B)** Percentage of clones showing punctiform KDEL-RFP signals in control (Ctrl, *n* = 10), *fzr-OE* (*n* = 13), and *rux-OE* (*n* = 11) groups. Data are mean ± SEM, analyzed by one-way ANOVA across three groups. **** represents P value <0.0001. **(C)** Confocal images of *lacZ-OE*, *fzr-OE + lacZ-OE*, *fzr-OE + xbp1-OE*, or *rux-OE + lacZ-OE* or *rux-OE + xbp1-OE* clones (green) under *hhts>GFP*, stained with Hoechst (blue) and DHE (red). White dashed lines mark the A-P boundary. Scale bars: 20 µm.

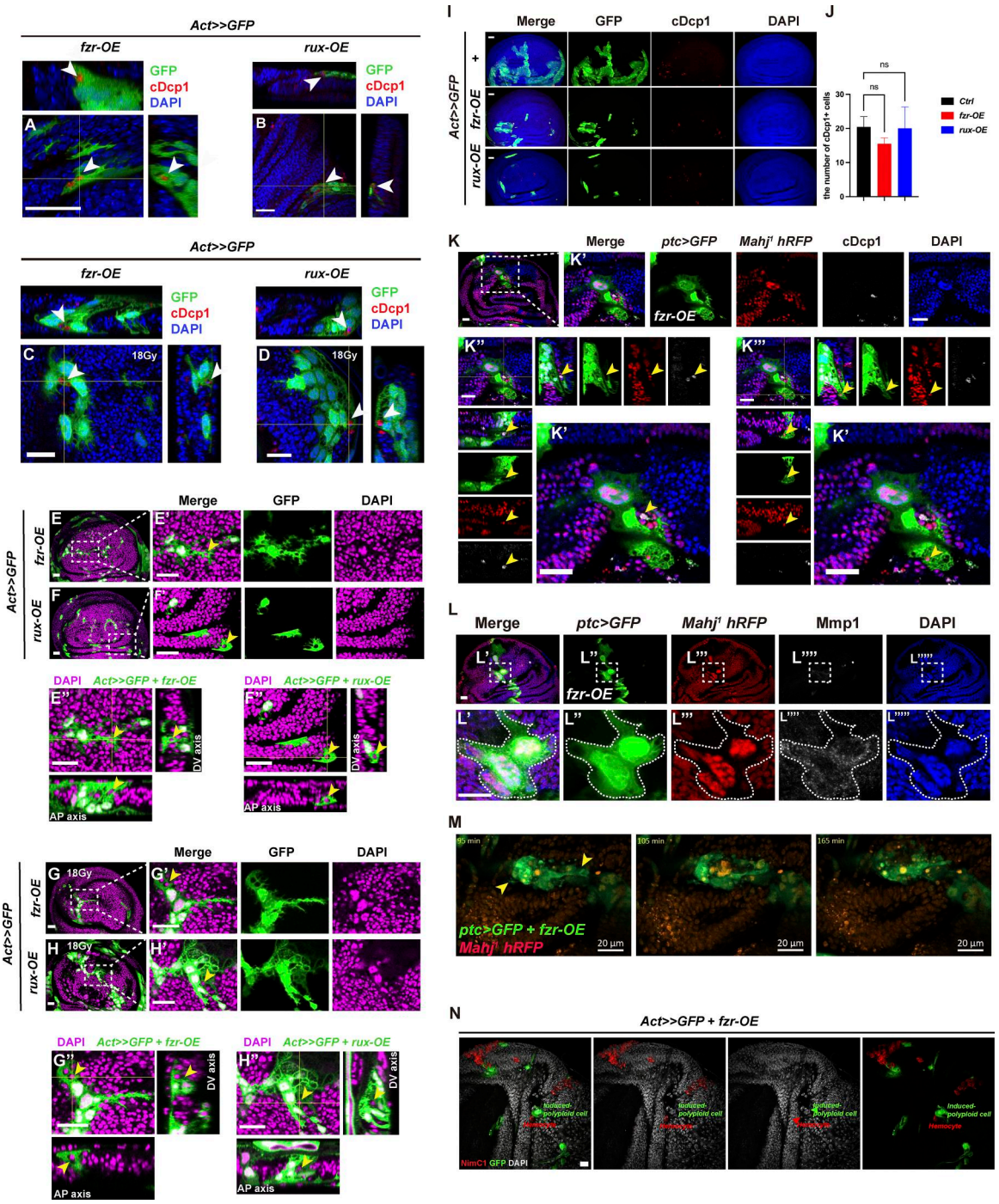

Figure S5. **Induced polyploid cells exhibit active engulfment. (A and B)** Confocal images of *fzr-OE* (A, wing disc) and *rux-OE* (B, eye disc) clones stained with cDcp1 (red) and DAPI (blue). **(C and D)** Confocal images of *fzr-OE* (C) and *rux-OE* (D) clones after 18 Gy γ-ray exposure, stained with cDcp1 (red) and DAPI (blue). White arrowheads indicate apoptotic (red) cells engulfed by green polyploid cells. Scale bars: 20 μm. **(E and F)** Single-plane confocal images of *fzr-OE* (E) and *rux-OE* (F) clones stained with DAPI (magenta). **(E′ and F′)** Zoomed-in views of white dashed rectangles in E and F, respectively. **(E″ and F″)** Orthogonal views of E′ and F′. **(G and H)** Single-plane confocal images of *fzr-OE* (G) and *rux-OE* (H) after 18 Gy γ-ray treatment. Stained with DAPI (magenta). **(G′ and H′)** Zoomed-in views of white dashed rectangles in G and H, respectively. **(G″ and H″)** Orthogonal views of G′ and H′. Yellow arrowheads indicate live cells engulfed by green polyploid cells. Scale bars: 20 μm. **(I)** Confocal images of *Act>>GFP* + control (Ctrl, +), *fzr-OE*, or *rux-OE* discs stained with DAPI (blue) and cDcp1 (red). **(J)** Quantification of the number of cDcp1-positive (cDcp1+) cells in ctrl (n = 15), *fzr-OE* (n = 10) and *rux-OE* (n = 4) groups. Scale bars: 20 μm. **(K)** Imaginal wing discs of *fzr-OE* induced by *ptc>GFP* (green) in a *mahj*^{1} (red) background, stained with cDcp1 (gray) and DAPI (blue). Yellow arrows indicate cells engulfed by *fzr-OE* cells. Scale bars: 20 μm. **(L)** Imaginal wing discs of *fzr-OE* induced by *ptc>GFP* (green) in a *mahj*^{1} (red) background, stained with Mmp1 (gray) and DAPI (blue). White dashed rectangle highlights *fzr-OE* + *mahj*^{1} cells showing JNK activation, marked by Mmp1 staining (gray). Scale bars: 20 μm. **(M)** Time-lapse images of *fzr-OE* induced by *ptc>GFP* (green) in a *mahj*^{1} (red) background. Yellow arrowheads indicate green cell protrusions contacting red cells. Scale bars: 20 μm. **(N)** Confocal images of imaginal wing discs with *fzr-OE* induced by *act>>GFP* (green), stained with DAPI (gray), NimC1 (red). Green arrowheads indicate *fzr-OE* cells; red arrowheads indicate hemocytes. Scale bar: 20 μm.

Video 1. **Time-lapse video of *fzr-OE* polyploid cell dynamics.** GFP-labeled *fzr-OE* (green) polyploid cells show dynamic behavior. Time-lapse imaging was performed using a 20× objective on a Zeiss 980 confocal microscope. 2-µm-thick z-sections, including the *fzr-OE* polyploid cell, were collected over 1,317 min at 6-min intervals. The video is played at 15 frames per second. Scale bar, 20 µm. Related to Fig. 1.

Video 2. **Time-lapse video of *rux-OE* polyploid cell dynamics.** GFP-labeled *rux-OE* (green) cells show dynamic behavior. Time-lapse imaging was performed using a 20× objective on a Zeiss 980 confocal microscope. 2-µm-thick z-sections, including the *rux-OE* polyploid cell, were collected over 1,316 min at 7-min intervals. The video is played at 15 frames per second. Scale bar, 20 µm. Related to Fig. 1.

Video 3. **Time-lapse video of *lacZ-OE* control cells.** GFP-labeled (green) lacZ-OE cells did not show obvious dynamics. Hoechst marked nuclei (blue). Time-lapse imaging was performed using a 20× objective on a Zeiss 980 confocal microscope. 2-µm-thick z-sections, including the *fzr-OE* polyploid cell, were collected over 245 min at 5-min intervals. The video is played at 15 frames per second. Scale bar, 20 µm. Related to Fig. 1.

Video 4. **Induced polyploid cells navigating around the trachea.** GFP-labeled *fzr-OE* (green) polyploid cell migrating around the trachea. Time-lapse imaging was performed using a 20× objective on a Zeiss 980 confocal microscope. 2-µm-thick z-sections, including *fzr-OE* polyploid cell, were collected over 898 min at 6-min intervals. The video is played at five frames per second. Scale bar, 20 µm.

Video 5. **Time-lapse video showing JNK activation in a *fzr-OE* polyploid cell.** TRE-RFP (red), marking JNK activity, shows dynamic changes in a polyploid cell (green). Time-lapse imaging was performed using a 20× objective on a Zeiss 980 confocal microscope. 2-µm-thick z-sections, including *fzr-OE* polyploid cell, were collected over 101 min at 3-min intervals. The video is played at five frames per second. Scale bar, 10 µm. Related to Fig. 3.

Video 6. **Time-lapse video showing JNK activation in *rux-OE* polyploid cells.** TRE-RFP (red), marking JNK activity, shows dynamic changes in *rux-OE* polyploid cell (green). Time-lapse imaging was performed using a 20× objective on a Zeiss 980 confocal microscope. 2-µm-thick z-sections, including *rux-OE* polyploid cell, were collected over 1,316 min at 7-min intervals. The video is played at 15 frames per second. Scale bar, 20 µm. Related to Fig. 3.

Video 7. **Time-lapse video showing *mahj*^{1} cells engulfed by *fzr-OE* polyploid cells.** GFP-labeled (green) *fzr-OE* cells are derived from ptc-Gal4 engulfing *mahj*^{1} cells (RFP, red). Time-lapse imaging was performed using a 20× objective on a Zeiss 980 confocal microscope. 2-µm-thick z-sections were collected over 898 min at 6-min intervals. The video is played at 15 frames per second. Scale bar, 20 µm. Related to Fig. 5.

Provided online is Table S1. Table S1 shows detailed genotypes for each experiment.